DESIGN AND ANALYSIS OF LIQUID-DROP ACCELEROMETER

by

Xu Wang

B.Eng. Beijing University of Chemical Technology, China, 2003

A THESIS SUBMITTED IN PARTIAL FULFILLMENT
OF THE REQUIREMENTS FOR THE DEGREE OF
MASTER OF APPLIED SCIENCE
in the School
of
Engineering Science

SIMON FRASER UNIVERSITY
Spring 2009

APPROVAL

Name: Xu Wang

Degree: Master of Applied Science

Title of thesis: Design and Analysis of Liquid-Drop Accelerometer

Examining Committee:

Dr. Albert M. Leung,
Professor, Engineering Science
Simon Fraser University
Chair

Dr. John D. Jones,
Associate Professor, Engineering Science
Simon Fraser University
Senior Supervisor

Dr. Bonnie Gray,
Assistant Professor, Engineering Science
Simon Fraser University
Supervisor

Dr. Ash M. Parameswaran,
Professor, Engineering Science
Simon Fraser University
SFU Examiner

Date Approved: March 23, 2009

Abstract

A novel design for a micromachined accelerometer is proposed. The working principle of the proposed design is detection of the movement of a liquid droplet in response to an imposed acceleration. When the acceleration is removed, the accelerometer is automatically re-set by the differential pressure of confined air cushions.

Experimental and numerical studies are used to evaluate the feasibility of the design, and to guide the selection of a suitable working fluid. Figures for sensitivity and response time are calculated, and the dependence of these performance parameters on working fluid properties is established. On the basis of these studies, a specific geometry, detection method and choice of materials is recommended, and a MEMS fabrication process for the device is outlined.

Acknowledgments

I would like to express my sincere gratitude to my senior supervisor Dr.John Jones for his endless supports, encouragement and patient guidance during my entire research. Not only did his insightful advice inspire my aspiration, but his such gentle manner also won all my respects and guided my behaviors in future.

My genuine thanks go to Dr.Albert Leung, Dr.Ash Parameswaran, and Dr.Bonnie Gray for their suggestions, wonderful lectures as well as patience. Their scrupulous attitudes and integrity really taught me how to be a qualified engineer.

I also acknowledge my former colleague Andy Wu and all my friends, Yifeng, Jinyun, Manu, Michael for their help and cooperation.

Nomenclature

A	Cross-sectional area, m^2
a	Acceleration, m/s^2
b	Damping coefficient, Kg/s
C	Capacitance, F
d	Diameter of tubes, m
d_m	Length of liquid-drop, m
E	Young's modulus, Pa
g	Gravity, g = 9.8 m/s^2
k	Spring constant, N/m
l	Tube length, m
p	Gas or fluid pressure, Pa
R	Resistance, Ω
t	Time, s
u	Fluid velocity, m/s
V	Potential difference, V
γ_{SV}	Surface tension of solid in contact with air, $dyne/cm$
γ_{SL}	Surface tension between and liquid, $dyne/cm$
γ_{LV}	Surface tension of liquid in contact with air, $dyne/cm$
ρ	Density, Kg/m^3
ϵ	Permittivity of the medium between plates
ϵ_0	Permittivity of vacuum
θ	Contact angle, degree
μ	Viscosity, Ns/m^2

Contents

List of Tables

List of Figures

Chapter 1

Introduction to Micromachined Accelerometer

High-resolution and wide-bandwidth microelectro-mechanical system (MEMS) accelerometers are increasingly demanded in military, aeronautic, seismic and acoustic applications [1]. Since the first micromachined silicon accelerometer was developed at Stanford University Integrated Circuit Laboratory for biomedical applications in 1978, it has been developed over 30 years. Since 1978, various microaccelerometers have been studied with different working principles and configurations. MEMS acceleration sensors are several orders of magnitude smaller than conventional ones and can be fabricated in large quantities by batch processing [10].

Conventional types of micromachined accelerometers generally include capacitive, piezoresistive, piezoelectric ones, etc. All of those accelerometers have been studied and developed into a very mature level, some have been mass-produced and gone into industrial market. Nowadays, a new generation of microaccelerometers with high-performance characteristics including low noise, high sensitivity, small drift, excellent stability and low temperature sensitivity has been widely investigated. Accuracy and operating range are the most challenging requirements [14].

1.1 Some Designs of Conventional Micromachined Accelerometers

The conventional field of MEMS accelerometers can be segregated into two dominant microsystem architectures: capacitive and piezoresistive. Although both types of accelerometer employ internal proof masses that are excited by acceleration, the architectural differences are in the transduction mechanism used to transform the displacement to an electrical signal. Capacitive accelerometers employ a differential capacitor whose balance is disrupted by the movement of the proof mass. Piezoresistive accelerometers generally rely on strain induced within a flexural element that attaches the proof mass to the sensor housing for identification of the mass movement. A schematic of a simple single-axis linear accelerometer is shown in Fig 1.1 [9]. The inertia of the proof mass restrains the motion of this element in the presence of an external force F_{ext} acting on a reference frame to which the proof mass is attached by means of a spring. The proof mass is subject to damping from the surrounding gas or from internal dissipation in the spring. The differential equation for the displacement x as a function of F_{ext} is obtained from Newton's law [9]:

$$m\frac{d^2x}{dt^2} + b\frac{dx}{dt} + kx = F_{ext} = ma \tag{1.1}$$

In Equation 1.1, k and b are the spring constant and damping coefficient, respectively, and linear relations are assumed. The solution to this equation is a decaying oscillation shown in Figure 1.2.

1.1.1 Micromachined Capacitive Accelerometer

Capacitive-based microelectromechanical systems accelerometers are devices that measure acceleration based on a change in capacitance due to a moving plate or sensing element. They generally offer more sensitivity and more resolution than similar piezoresistive accelerometers. For most commercial applications, the maximum g-sensing level(MGSL) employed in capacitive accelerometer is 500g [4].

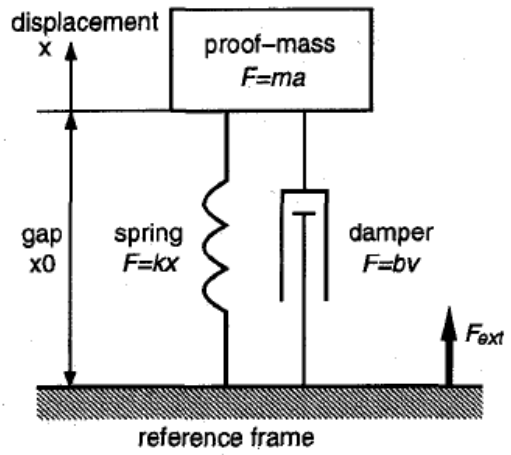

Figure 1.1: The Model of An Accelerometer [9]

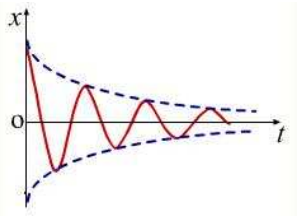

Figure 1.2: Decaying Oscillation

Fig 1.3 shows the schematic of the Endevco 7290-A capacitive accelerometer [4].

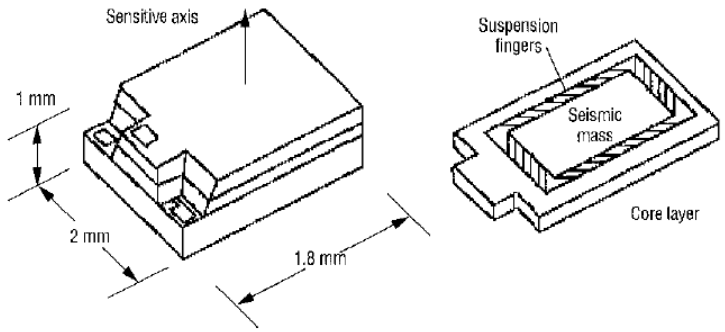

Figure 1.3: Schematic of the Endevco 7290-A [4]

This low-g sensor takes advantage of unique variable-capacitance microsensors in its design. The Endevco 7290-A uses gas damping and internal over-range stops to allow the silicon microsensors to withstand high acceleration loads and shock. With an MGSL of $\pm 100g$ and a typical sensitivity of $20 \pm 10mV/g$, these accelerometers were designed to detect small acceleration changes in automotive and aerospace environments.

The output of the device is obtained from a half bridge capacitive acceleration sensor. Positive acceleration causes the capacitance between the seismic mass and the base to increase, while the capacitance between the seismic mass and lid decreases. A typical capacitive sensitivity is about $0.06 \pm 0.03pF/g$.

1.1.2 Piezoresistive-Based Accelerometer

The piezoresistive effect is the phenomenon in which the electrical resistance of a material changes due to applied stress. Applied stress changes the energy band structure,

leading to a resistivity change that can be explained in terms of holes transfer and mass shift phenomena. The strain experienced by a piezoresistive material causes a position change of its internal atoms, resulting in the change of its electrical resistance.

The use of piezoresistive materials in the design of MEMS-based accelerometers was first proposed by Roylance and Angell(1979) discussed in [15]. Their design calls for a proof mass attached to a silicon housing through a short flexural element. The implantation of a piezoresistive material on the upper surface of the flexural element was used for measuring out-of-plane acceleration of the proof mass. By completing a Wheatstone bridge around the piezoresistors of the accelerometer, a linear relationship between acceleration and voltage can be derived.

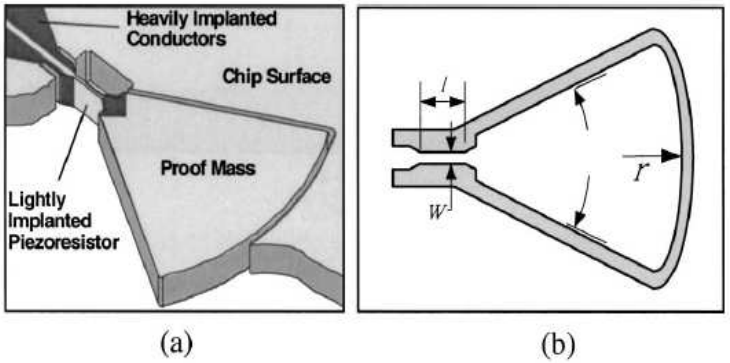

Figure 1.4: Piezoresistive Accelerometer Design Illustration, Physical Dimensions[15]

Jerome and Aaron discussed in [15], explored a new approach to piezoresistive accelerometer. Departing from the Roylance design, they examined a lateral in-plane accelerometer that can exploit the use of Deep Reactive Ion Etching (DRIE) fabrication techniques. The design of the planar accelerometer is straightforward. A pie-shaped proof mass, as shown in Figure 1.4(a), is attached to the sensor housing

through a slender cantilevering element. Acceleration in the plane of the sensor will cause deflections in the proof mass and flexural element. Implanted in the walls of the cantilevering element is a piezoresistive material that will change resistance with strain. The flexural element is designed to concentrate strain in the vicinity of the piezoresistive implant. The housing surrounding the proof mass provides a lateral stop on the mass movement, thereby setting the maximum measurable acceleration. This housing is advantageous because it prevents deflections that would result in non-linear flexural responses in addition to protecting the accelerometer from shock. The physical dimensions of the accelerometer are illustrated in Fig. 1.4(b). The flexural width w is minimized when the radial length r of the proof mass is maximized. The bandwidth of the accelerometer is determined from the length of the flexural element l, with shorter flexural elements increasing the lateral resonant frequency of the sensor.

1.1.3 Bulk-Micromachined Piezoelectric Accelerometer

Accelecrometers based on the piezoelectric effect are widely employed in many practical applications. Their main features are low damping, high output impedance, wide operating temperature range (up to 300 °C) and high Q (indicating a lower rate of energy dissipation relative to the oscillation frequency) [7]. A typical piezoelectric accelerometer consists of a layer of piezoelectric material sandwiched between a mounting plate and a seismic mass. When a force or a pressure is applied to the opposite faces of the piezoelectric material, an electric charge is produced. This charge can be amplified to give an output voltage that is proportional to the applied force or acceleration.

The schematic diagram of piezoelectric accelerometer is shown in Fig 1.5 [11]. When the cantilever is forced with a vertical load in the center of mass block, the deflection equation of the cantilever can be expressed as

$$\varepsilon(x) = \frac{3(l_c + l_m/2)x^2 - x^3}{6EI_y} F_z \qquad 0 \le x \le l_c \tag{1.2}$$

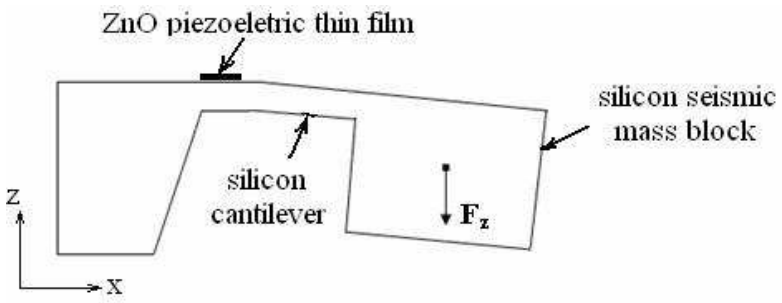

Figure 1.5: The Principle of Piezoelectric Accelerometer [11]

where E is Young's modulus, I_y the rotary inertia of the cantilever, l_c and l_m the length of cantilever and mass block, respectively. And the deflection δ and angle θ at $x = l_c$ are

$$\delta = \varepsilon(l_b) = \frac{4l_c^3 + 3l_c^2 l_m}{12EI_y} F_z \theta = \varepsilon^{'}(l_b) = \frac{l_c^2 + l_c l_m}{2EI_y} F_z \tag{1.3}$$

When the accelerometer works, the force acting on mass block leads to deflection of the cantilever, and maximum stress occurs at the fixed end of the cantilever. The ZnO piezoelectric thin film is therefore sputtered and patterned on the fixed end of the cantilever, generating an electric potential that is proportional to the force applied on the mass block.

1.2 Some Novel Designs of Unconventional Micromachined Accelerometers

1.2.1 Micro-Opto-Mechanical Accelerometer

In [25] Dr Lee and Cho presented a lateral micro-opto-mechanical accelerometer, characterized by its movement being parallel to the sensing axis. It uses a single-mode optical fiber and a laser diode as a light source. The micro-accelerometer part consists of a seismic mass, suspended by vertical silicon beams, and a shutter that is located

between two single-mode optical fibers. During acceleration, the shutter moves laterally and modulates the light intensity reaching the photo diode. The photodetector converts the light intensity into a DC voltage [25].

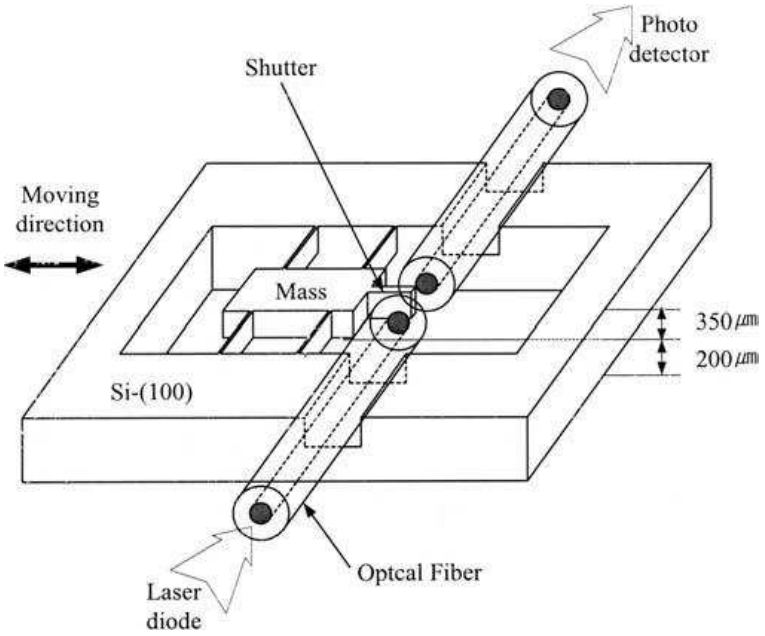

Figure 1.6: The Schematic Diagram of Micro-Opto-Accelerometer [25]

Figure 1.6 shows a schematic drawing of the accelerometer. It consists of a seismic mass and four thin vertical beams. Since these four beams restrict the mass's movement along the one direction illustrated in the figure, it ensures the accuracy of signal. When acceleration in that direction is applied, the shutter will block the light intensity as same frequency as the acceleration, then photo detector records and sends as output. Fig.1.7 is taken from the real prototype fabricated by DRIE technology. Based on the principle and structure of this micro-opto-mechanical device, it is widely used to monitor machining states with a simple detection principle.

1.2.2 Convection-Based Micromachined Accelerometer

The principle of the convention-based micromachined accelerometer is the measurement of temperature changes. When electrical current goes through a centrally located

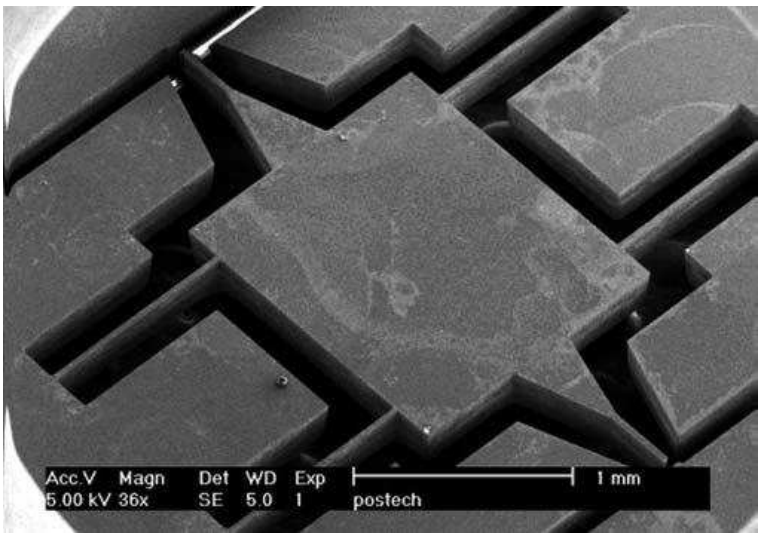

Figure 1.7: SEM Picture of Micro-Opto-Accelerometer [25]

polysilicon heater, a temperature profile is generated around the heater. If acceleration equals zero, two thermometers placed symmetrically on both sides of the heater, shown in Figure 1.8, sense the the same temperature. So the temperature profile is evenly divided by Y-axis. If an acceleration is applied, due to the buoyancy force the temperature profile is distributed differentially on both sides of the heater. This convective accelerometer is good at detecting constant as well as oscillatory acceleration.

Compared with other types of MEMS accelerometers, the most significant highlight of this design is high survivability. Because inside the structure only the heated fluid is moved by external acceleration, unlike proof-mass structure, so it is capable of bearing more acceleration than those with proof-mass. The sensitivity of the convective accelerometer can achieve up to 100 mV/g when air is used as working fluid, much higher than ADXL 50 with a sensitivity of 20 mV/g. If the air is replaced by a liquid or a higher pressure air, the sensitivity of convective accelerometer can be increased two to three orders of magnitudes [5].

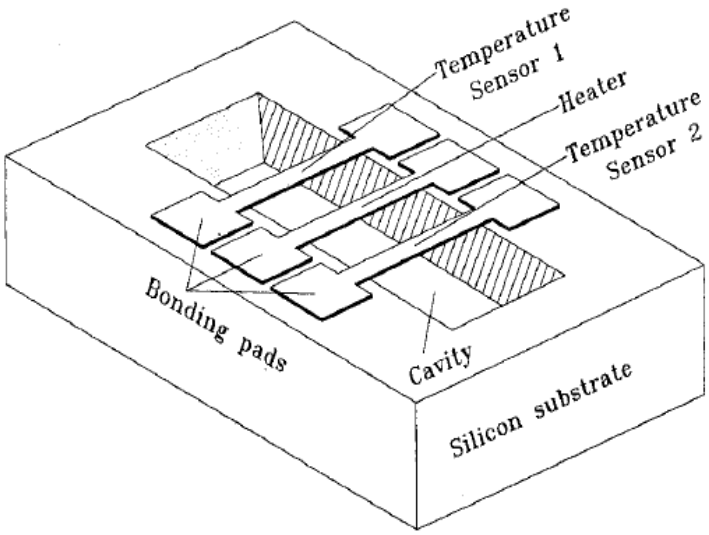

Figure 1.8: The Structure of Thermal Accelerometer [2]

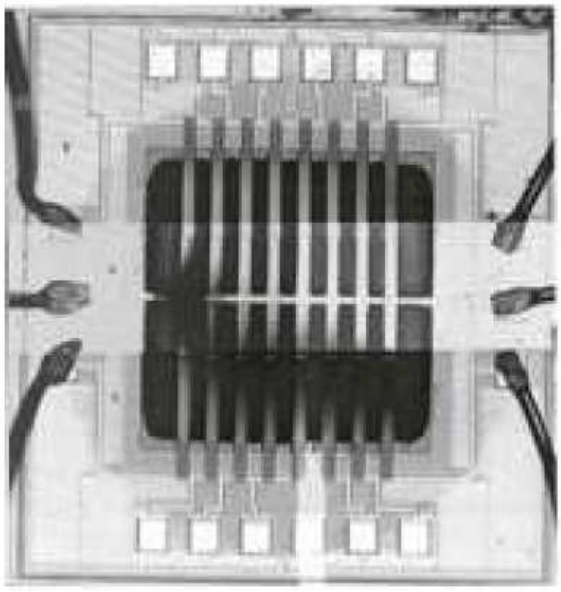

Figure 1.9: A Image of Convective Accelerometer Chip [2]

1.3 Summary

Despite the large number of existing accelerometer designs, the invention of the convection-based accelerometer shows that there is still scope for the invention of new designs based on new physical mechanism. Such new designs may have unique advantages, such as high survivability. That is a motivation for this research project. The following contents document our new design using liquid-droplet as a proof-mass.

Chapter 2

Liquid-Drop Accelerometer Design

Proof-mass-based microaccelerometers, known as conventional types, have been applied in many areas. However, they have limitations such as relative vulnerability and limited measurement range. Our research will explore unconventional accelerometers, using liquid as working fluid. In this chapter, we are going to introduce the fundamental design and theory for accelerometers of this type.

2.1 Liquid-Drop Structure

A new proposed design in this chapter is to minimize the limitations of the proof-mass accelerometer while maximizing its advantages: A liquid droplet, functioning as proof-mass, placed in a duct confined by gas cushions is proposed, shown in figure 2.1. In this duct, a liquid drop is confined in the middle and air cushions occupy both ends with the same pressure enclosing the droplet. In this structure, the gas cushions function as springs balancing their pressure with outside force on the proof-mass (liquid droplet). One advantage of using gas cushions in place of mechanical springs is that they are more robust, unbreakable, and not subject to fatigue. When an acceleration acts parallel to the axis of the tube, the droplet moves until differential pressure of the gas cushions balances the acceleration.

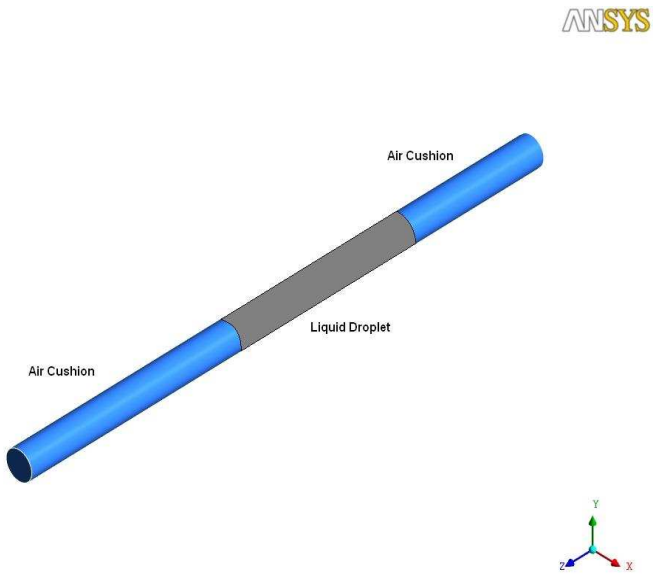

Figure 2.1: The Schematic Diagram of Liquid Proof Mass

2.2 Possible Methods of Measurement

Three methods of detecting the droplet motion have been proposed for this project: pressure-sensor, resistive and capacitive measurement. In the following sections, each of them will be reviewed from working principles, liquid requirements, advantage and disadvantage.

2.2.1 Pressure Sensor Measurement

In this design, a pressure sensor is placed at each end of duct. When the droplet moves under external acceleration, in order to balance the force both gas cushions create a differential pressure. In other words, one gas cushion will be squeezed by liquid droplet to produce higher pressure than static state, the other will be released to decrease pressure. The two pressure sensors will record the pressure on each side respectively. Therefore, the value of acceleration could be obtained by calculations.

$$(P_1 - P_2)s = ma \tag{2.1}$$

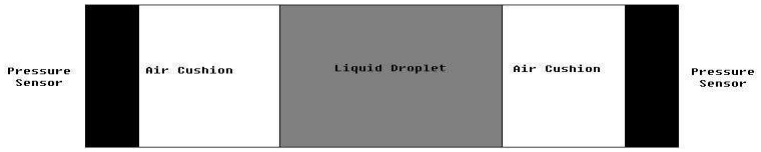

Figure 2.2: The Model of Pressure Sensor Accelerometer

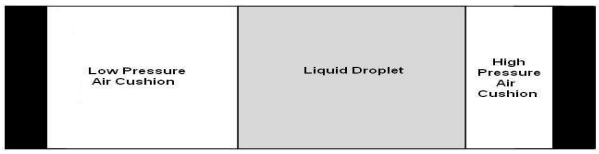

Figure 2.3: Accelerated Pressure Sensor Accelerometer

$$\Longrightarrow a = \frac{(P_1 - P_2)s}{m} \tag{2.2}$$

$$\Longrightarrow a = \frac{P_1 - P_2}{\rho \cdot L} \tag{2.3}$$

Where:
P_1, P_2: Pressure detected by sensors at each end
s: Cross-section area of inner duct
m: Mass of the liquid droplet
ρ: Density of the liquid
L: Length of liquid-drop

Although this method is theoretically possible, this requires measuring very small differential pressures - of the order of a few pascals. Fabricating reliable and accurate pressure sensors would be a challenge.

2.2.2 Capacitive Measurement

Capacitive measurement can be achieved by two pairs of capacitors on each side of duct, while liquid-drop stays in the middle of duct. The two capacitors would be connected to outside meters, as in figure 2.4.

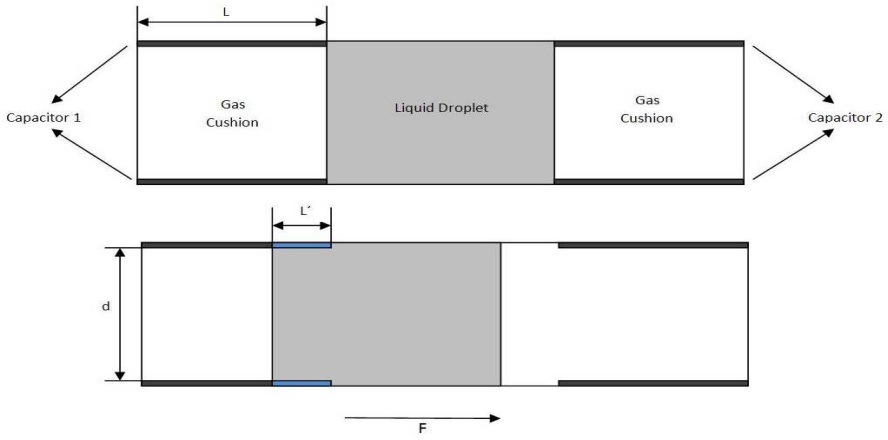

Figure 2.4: The Model of Capacitive Sensor Accelerometer

The capacitance of a parallel-plate capacitor is given by:

$$C = \epsilon \cdot \frac{A}{d} = \frac{\epsilon_r \cdot \epsilon_0 \cdot A}{d} \tag{2.4}$$

Where:

C: the value of capacitance

ϵ: the permittivity of the medium between the plates

A: the area of each plate

d: the separation between the plates

The permittivity of a material is usually given relative to that of vacuum, as a relative permittivity ϵ_r. The actual permittivity is then calculated by multiplying the relative permittivity with the permittivity of vacuum, ϵ_0:

$$\epsilon = \epsilon_r \cdot \epsilon_0 \tag{2.5}$$

The permittivity of air is close to that of vacuum. When there is no acceleration on the device, droplet firmly stays in the middle without any contacts with either capacitance. Hence

$$C_1 = C_2 = \epsilon_0 \cdot \frac{A}{d} \tag{2.6}$$

After the droplet moves, we have the situation shown in Fig 2.5.

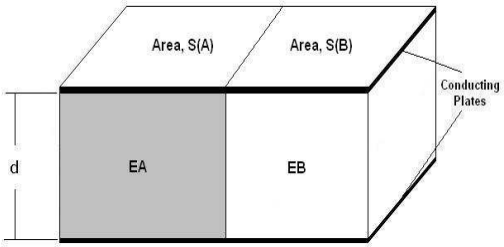

Figure 2.5: Vertical Dielectric Interface

For E_A and E_B in Fig 2.5, they have the same distances between two plates, occupies areas of S_A, S_B. Then an assumed potential difference would produce the same strengths. Therefore,

$$C' = \frac{\epsilon_A S_A + \epsilon_B S_B}{d_2} = C_A + C_B \tag{2.7}$$

When a certain acceleration exists, for instance, the resulting configuration is shown in the lower half of Fig 2.4. C_2 still has not changed.

$$C_2 = \epsilon_0 \cdot \frac{A}{d} \tag{2.8}$$

However:

$$C_1 = \epsilon_0 \cdot \frac{(L - L') \cdot s}{d} + \epsilon_0 \cdot \epsilon_r \cdot \frac{L' \cdot s}{d} \tag{2.9}$$

$$C_1 = \epsilon_0 \cdot \frac{s}{d} \cdot ((L - L') + \epsilon_r \cdot L') = \epsilon_0 \cdot \frac{s}{d} \cdot (L + (\epsilon_r - 1) \cdot L') \tag{2.10}$$

Therefore,

$$L' = \frac{\frac{C_1 \cdot d}{\epsilon_0 \cdot s} - L}{\epsilon_r - 1} \tag{2.11}$$

So from the value of capacitance measured, the distance that liquid-droplet moves can be calculated. Then acceleration can be calculated. An exact formula for this is derived in Chapter 3 Equation 3.8 - 3.10.

A further complication is that the inner surface of the duct may need to be coated with a low-friction material such as Teflon, giving the situation shown in 2.6.

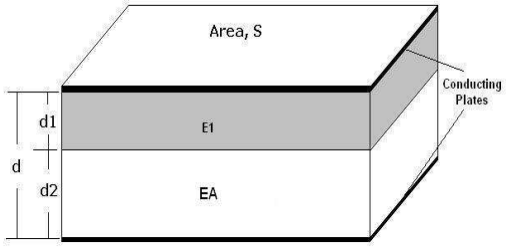

Figure 2.6: Parallel Dielectric Interface

As shown, how would capacitance change if there are multiple kinds of dielectrics between two plates? For parallel dielectrics E_1 and E_A in Fig 2.6, they split the potential between two conducting plates, so:

$$C = \frac{Q}{V} = \frac{Q}{V_1 + V_A} = \frac{1}{\frac{d_1}{\epsilon_1 S} + \frac{d_2}{\epsilon_A S}} = \frac{1}{\frac{1}{C_1} + \frac{1}{C_A}} \tag{2.12}$$

When using capacitance as a detecting method, there are a few requirements for selecting the proper liquid.

• The liquid must be dielectric, preferably with a high dielectric constant. Because the higher dielectric constant it has, the stronger signal is measured.

• The liquid must be in very stable state, not easy to evaporate or freeze, especially when ambient temperature varies from $-20\,^{\circ}\mathrm{C}$ to $100\,^{\circ}\mathrm{C}$. Otherwise, the sensor decreases its accuracy when temperature changes its state.

• For the considerations of mass fabrication in future, the liquid is preferred to be non-toxic and low-cost.

• The liquid is able to move without wetting wall in the duct. If the wall of duct attracts liquid, the droplet will be attenuated, resulting in inaccuracy.

As a proof of concept, a parallel-plate capacitor test rig was constructed and the change in capacitance measured as the space between the plates was filled with methanol, a high-dielectric fluid. Even for this relatively large capacitor, the change in capacitance was of the order of a few nanofarads. It was deduced that the change in capacitance expected from a micromachined accelerometer would be on the picofarad or femtofarad scale. Capacitance changes on this scale can nevertheless be measured: it is important to convert the capacitance change to a change in the frequency of an AC circuit at the initial stage, then to measure this change in frequency.

2.2.3 Resistive Measurement

Mercury Switch

In the early twentieth century, the mercury switch was widely used as a tilt sensor in many areas, due to its simple structure. It consists of a sealed glass tube containing two unconnected electrodes and a small bead of mercury. As long as the liquid metal remains on the opposite end of the tube, the electrodes remain disconnected and no current will flow. Once the tube is moved over a certain angle, the mercury will pool between the two electrodes and a connection is formed, as a result electricity

Figure 2.7: Mercury Switch

flows through a completed circuit. After the liquid metal has returned to its original position, the electrical current stops immediately. Figure 2.7 is a single-pole mercury switch.

Design of Resistive Measurement

The mercury-switch method can be adapted to give a quantitative measure of acceleration by implanting two pairs of unconnected conductors on each side of the duct. When the device is in static state, the droplet is sitting in the middle of duct, connecting both conductors, so that a certain electrical current goes through. When liquid droplet is displaced by the acceleration, the two conductors are immersed deeper in the liquid. The higher acceleration is, the further the liquid droplet moves towards the end, the shorter the resistance of two conductors become. Therefore, through measuring resistance of the conductors, acceleration is obtained. Please see Figure 2.8.

According to:

$$V = I \cdot R = I \cdot \frac{l \cdot \rho}{A} \tag{2.13}$$

$$\Longrightarrow \frac{V}{I} = \frac{l}{A} \cdot \rho = R \tag{2.14}$$

Where:

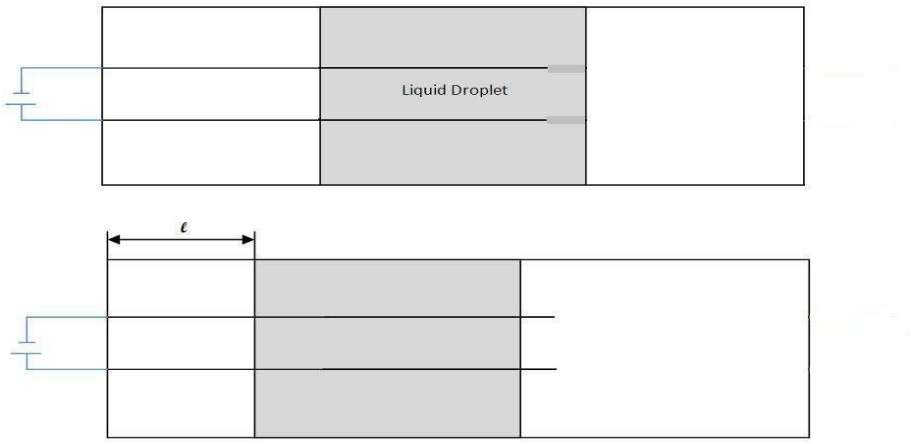

Figure 2.8: The Model of Resistive Sensor Accelerometer

V: the potential difference across conductors
I: the current through conductors
R: the resistance of conductors
l: the length of conductor
A: the cross section area of conductor
ρ: the resistivity of the material of conductor

For liquid selection, it demands that liquid is conductive, and does not adhere to the wall, for which mercury is the first choice, because of its high conductivity as a liquid metal.

Chapter 3

Theoretical Background

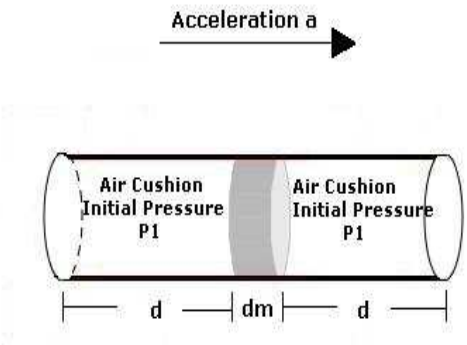

Figure 3.1: Dimension of Liquid Droplet In Duct

3.1 Theoretical Calculation

When a certain acceleration is applied to the accelerometer, the distance that liquid is driven can be calculated. Compression and rarefaction of the gas is assumed to be isothermal, this assumption becomes increasingly accurate as the size of the accelerometer is decreased.

According to ideal gas law, the following equations are used to describe the pressure and volume change before and after acceleration is applied:

$$P_1 \cdot V_1 = P_2 \cdot V_2 = P_3 \cdot V_3 \tag{3.1}$$

Where:
P_1, V_1 = the initial pressure and volume of gas cushion
P_2, V_2 = the pressure and volume of left-side gas cushion after applied acceleration
P_3, V_3 = the pressure and volume of right-side gas cushion after applied acceleration

Initially the droplet is right in the center of duct, having the same distance, d, from both ends. When droplet is driven by a rightwards acceleration, it is displaced x towards the left end. Correspondingly, the left gas cushion is compressed by droplet and its pressure P_2 can be expressed in Equation 3.2, while the right gas cushion is elongated and its pressure P_3 can be expressed in Equation 3.3.

$$P_2 = \frac{V_1}{V_2} \cdot P_1 = \frac{d}{d-x} \cdot P_1 \tag{3.2}$$

$$P_3 = \frac{V_1}{V_3} \cdot P_1 = \frac{d}{d+x} \cdot P_1 \tag{3.3}$$

Where:
d: the initial length of gas cushion on the left and right sides

The liquid droplet stops at the position where the acceleration force is balanced by the differential pressure between the two gas cushion. According to Newton's Second Law:

$$F = m \cdot a = (P_2 - P_3) \cdot A \tag{3.4}$$

$$\rho \cdot d_m \cdot A \cdot a = (P_2 - P_3) \cdot A \tag{3.5}$$

$$\Longrightarrow \rho \cdot d_m \cdot a = P_2 - P_3 \tag{3.6}$$

Where:
ρ: the density of working fluid
d_m: the thickness of liquid droplet
a: the acceleration applied to the accelerometer
A: the cross-section area of channel

Substituting Equation 3.2 and 3.3 into Equation 3.5:

$$\rho \cdot d_m \cdot A \cdot a = (\frac{d}{d-x} - \frac{d}{d+x}) \cdot P_1 \cdot A \tag{3.7}$$

Define the dimensionless parameter C:

$$C = \frac{\rho \cdot d_m \cdot a}{P_1} \tag{3.8}$$

Hence Equation 3.7 can be simplified to:

$$Cx^2 + 2dx - Cd^2 = 0 \tag{3.9}$$

The positive root of equation 3.9 is:

$$x = \frac{d(\sqrt{1+C^2} - 1)}{C} \tag{3.10}$$

To get an idea of the size of x, we consider a possible design. If mercury is considered as the working fluid in an accelerometer with the following dimensions:

• The total length of micro-channel is 30 mm, in which the thickness of the mercury droplet d_m is 10 mm and each gas cushion d is 10 mm long.

• The initial pressure of both gas cushions is 2000 Pa.

• The applied acceleration is $9.8m/s^2$, which can be achieved by tilting the micro-channel from horizontal to vertical position.

Based on the above defined parameters, C value is calculated from the following equation:

$$C = \frac{\rho \cdot d_m \cdot a}{P_1} = \frac{13579 \times 10 \times 10^{-3} \times 9.8}{2000} = 0.665 \tag{3.11}$$

The moving distance of droplet is calculated from equation 3.10:

$$\begin{aligned} x &= \tfrac{d(\sqrt{1+C^2}-1)}{C} \\ &= \tfrac{10\times10^{-3}\times(\sqrt{1+0.665^2}-1)}{0.665} \\ &= 3.021mm \end{aligned} \tag{3.12}$$

The expected displacement of the droplet is a few millimeter, which is detectable. Any other working fluids with lower density than mercury or higher gas cushion pressure will move smaller distance. Therefore, reduced-pressure cushions and high density fluids should be considered.

Equation 3.8 shows that the initial pressure of both air cushions directly impacts the distance which liquid droplet can travel. The less pressure air cushions have, the further liquid droplet can move, and the more sensitive the accelerometer is. If the sealed air cushion is at 100,000 Pa, the displacement for the mercury modeled in Equation 3.10 is 6.65 μm. Keeping all other parameters the same and dropping air cushion pressure to 2000 Pa, the distance that mercury can move is increased by 450 times, which greatly improves the sensitivity.

Due to the vapor pressure of the working fluids, the pressure of air cushion can not be decreased without limitation. Otherwise, some liquids would turn into vapor,

seriously impairing accuracy.

3.2 Sensitivity And Response Time Calculation

In the preceding chapter, we have outlined several different possible designs for detecting acceleration based on the motion of a liquid drop confined between air cushions. In the remainder of the thesis, we will use numerical simulation and experiment to refine these designs, identify the material properties that we would like the working fluid to have, and predict how each of these properties will affect the sensitivity and response time of the accelerometer.

3.2.1 Device Sensitivity

Some of the factors influencing the sensitivity of the device have been analyzed in Equations 3.4 to 3.12, where it has been shown that the distance the droplet moves in response to an applied acceleration is given in Equation 3.10:

$$x = \frac{d(\sqrt{1+C^2}-1)}{C}$$

where C is the dimensionless group $\rho \cdot d_m \cdot a/P_1$. This function is plotted as a function of C in Figure 3.2. From this we can deduce that sensitivity is increased by choosing a dense fluid. We also note that P_1, the initial pressure of the gas cushions, is bounded below by the vapor pressure of the working fluid. Thus, to maximize sensitivity, we seek a fluid with a low vapor pressure. This graph illustrates a strength of this design, which is that it behaves well even if subjected to very high accelerations - it can still measure them, it just becomes less sensitive (because the graph is flatter). So potentially it is an even more robust design than the Leung hot-air accelerometer[5], since this contains suspended beams which can break under high stress or fatigue under vibrational stress.

An additional determinant of sensitivity will be the fluid's permittivity (if the fluid

motion is detected via capacitance) or its conductivity (if the fluid motion is detected via conduction).

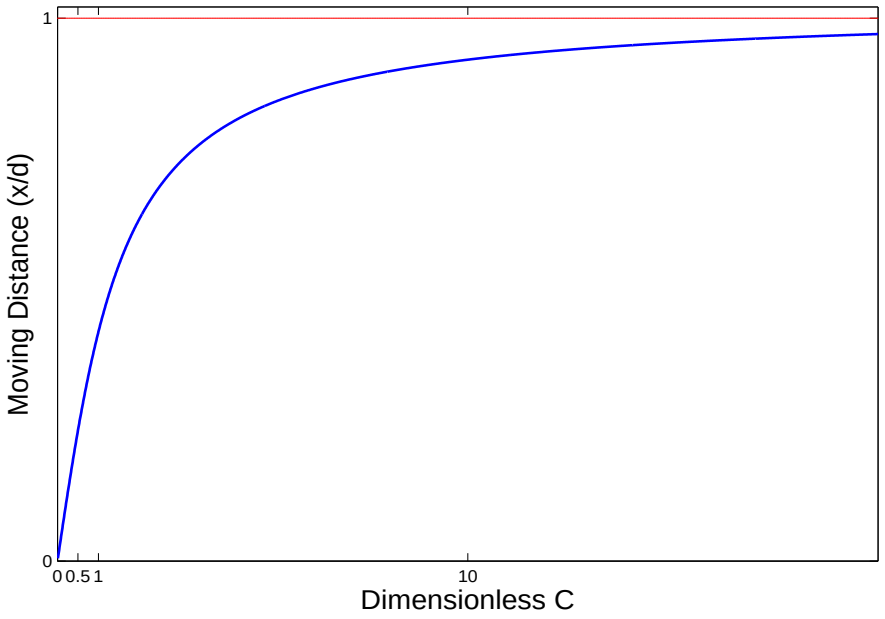

Figure 3.2: Function of C

3.2.2 Device Response Time

It will be shown in Chapter 4 that, when an acceleration is imposed, the liquid drop will move towards one end of the tube, and then pass through several oscillations about its new equilibrium position before coming to rest. We will calculate the time taken for this to happen in a particular case using numerical simulation. However, the simulation, using the package 'CFX', takes a number of days to converge, so it is not practical to simulate a large number of different geometries and working fluids. Instead, we use a simpler, approximate method to estimate response times, then argue that the actual response times will vary in proportion to their estimates.

The argument we use is as follows:

For a given fluid and geometry, we can calculate the distance we expect the fluid droplet to move, using Equations 3.4 to 3.12. We can also calculate the terminal velocity of the fluid in a circular duct of the given dimensions, using Poiseuille's equation for fluid friction in laminar flow,

$$u = \frac{\Delta p d^2}{32 \mu l} \tag{3.13}$$

where u is the fluid velocity, $\Delta p/l$ the pressure gradient, and μ the fluid viscosity. The pressure gradient producing movement is simply the hydrostatic pressure gradient resulting from the imposed acceleration, $\rho g l$, where ρ is the liquid density, g the imposed acceleration, and l the length of the droplet. Thus we have:

$$u = \frac{\rho g d^2}{32 \mu} \tag{3.14}$$

as our estimate of terminal velocity. The estimated response time will therefore be:

$$t = x/u \tag{3.15}$$

where x is the distance the droplet moves.

For ducts of square or other cross-section, Poiseuille's formula must be modified. We use the formula developed by Bahrami *et al.* in [22].

$$u = \frac{\Delta p c^2}{\mu l}\left(\frac{1}{3} - \frac{64}{\pi^5}\frac{c}{b}\tanh(\pi b/2c)\right) \tag{3.16}$$

where b and c are the half height and half width of a tube of rectangular cross-section. Again replacing the pressure gradient with the hydrostatic pressure and putting $b = c$, this becomes:

$$u = \frac{\rho g c^2}{\mu}\left(\frac{1}{3} - \frac{64}{\pi^5}\tanh(\pi/2)\right) \tag{3.17}$$

In Chapter 5 we compare the predictions of these formulae with experiment, and in Chapter 4 we compare them with the results of CFX simulation. This is a useful check both on the formulae and on the reliability of the CFX package.

3.3 Capillarity and Surface Tension

For a small liquid droplet, there are two critical questions: will the liquid wet the glass and will the droplet hold together? Contact Angle and Surface Tension are two important properties determining liquid behavior. Contact Angle is a quantitative measure of the wetting of a solid by a liquid. It is defined geometrically as the angle formed by a liquid at the three-phase boundary where a liquid, gas and solid intersect, as shown in Figure 3.3. Surface Tension is the force that holds the interface together.

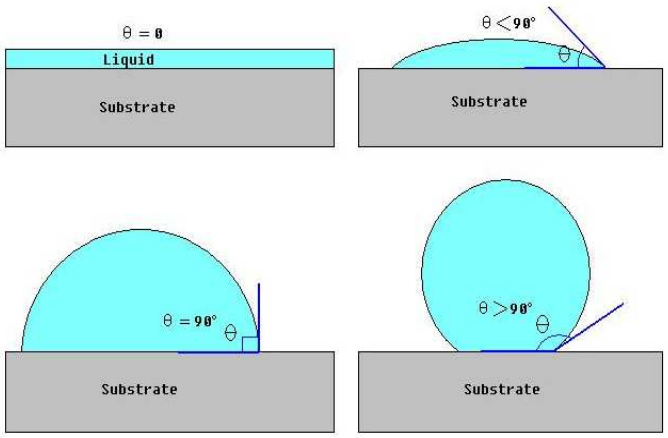

Figure 3.3: Three kinds of Contact Angles

In general, wettability is the ability of a liquid to adhere to a solid and spread over its surface to varying degrees. The classical model provided by Thomas Young suggests that[19]:

$$\gamma_{SV} = \gamma_{LV} cos\theta + \gamma_{SL} \tag{3.18}$$

Where:
θ is the contact angle
γ_{SV} is the surface tension of the solid in contact with air
γ_{SL} is the surface tension between the solid and the liquid

The work of adhesion W_a between the solid and liquid can be expressed in terms of the Dupre equation as follows:

$$W_a = \gamma_{SV} + \gamma_{LV} - \gamma_{SL} \tag{3.19}$$

A combination of the Young-Dupre equation gives:

$$W_a = \gamma_{LV}(1 + cos\theta) \tag{3.20}$$

From Equation 3.20, the liquid will wet the surface if W_a is greater than γ_{LV}, that means that the contact angle is smaller than 90°. In order to reduce adhesion, we want the contact angle greater than 90°. Hence W_a becomes smaller.

At the molecular level, there are two phenomena: Cohesion and Adhesion. Molecules in the liquid state experiences strong intermolecular attractive forces. When those are between the same kind of molecules, they are referred to as cohesion. When the attractive force are between different kinds of molecule, they are said to be adhesion. Note that most circumstances have both cohesion and adhesion occurring but one is normally stronger than the other. When adhesive forces between liquid molecules

and the walls of a glass tube are stronger than the cohesive force, the liquid forms an upward turning meniscus at the wall of the vessel and a capillary rise will occur. Therefore we are looking for a liquid that has high cohesion - so the droplet remains intact - and a liquid-solid combination that has low adhesion, so the liquid does not wet the surface.

The effect of capillarity is important because we are working on the micro-scale. Unlike viscous fluid friction, capillary effects arise because of the difference between the fluid's attraction for itself compared with its attraction for the walls of the duct.

The contact angle between the fluid and the inner surface of the duct is an important parameter. If this angle is less than 90°, the fluid will wet the surface and the device will not function. (This has been verified using CFX simulation.) This consideration limits the feasible combinations of working fluid and duct material. However, we have been able to identify a number of non-wetting fluid/duct combinations, as will be discussed in Chapter 6.

Chapter 4

Numerical Studies

In this chapter, an ANSYS CFX model of liquid-droplet accelerometer is constructed for numerical simulations. Throughout the simulation study, the liquid-droplet was modeled and located in the middle of the duct, while gaseous working fluid was modeled and filled the rest of space of the duct.

One of the important observations during simulation, the track of liquid-droplet's movement, is analyzed. By setting different parameters or critical values, the performance of the accelerometer with selected working fluids is documented. The result confirms our original assumption and design.

4.1 ANSYS CFX Transient Analysis

The first simulation by ANSYS CFX is to simulate a transient model: In an airtight tube, a selected working fluid is in the middle and air cushions with a certain pressure are on both sides. When an acceleration is applied on the whole tube, the fluid movement and all related data will be observed.

4.1.1 Parameter Settings

One reason that we want to use CFX to simulate this experiment is to confirm that fluid blob is able to hold together during movement. If it can achieve that for certain values of contact angle, surface tension, and tube diameter, it proves the possibility of our design.

As discussed in the previous chapter, to make our design work, we need to choose a fluid that meets all required standards, such as contact angle, surface tension and boiling and melting point. According to the discussion in Chapter 3, a contact angle over 90° is vital to prevent fluid bead from sticking on the wall, and the larger the contact angle the better. In Wu [2], mercury was mentioned as an ideal fluid with satisfying properties for simulation, such as 140° contact angle, low surface tension, high boiling point. It is a perfect fluid in this analysis.

In circular tubes, diameter of tube is also important to hold fluid together. Over a certain size of diameter, mercury can not cohere as a blob, which will be investigated experimentally in Chapter 5. In this simulation, a 3mm diameter circular tube is modeled. Experiment has shown that this is small enough to support a coherent blob.

4.1.2 CFX Model

The CFX Model of Liquid-droplet duct is shown in Figure 4.1. It is a 3-D cylinder, where the outside is a wall to constrain fluids. Liquid and air are specified in the duct. The total length is 30mm and 3mm diameter corresponding to the case modeled in chapter 3. The complete simulation procedures for setting up models and parameters are described in Appendix A. The mercury drop modeled in the center is 10mm in length. Besides contact angle, surface tension (0.48 N/m) and density were included. At both ends of the duct, air was modeled as 10mm long cushion at a pressure of 2000 Pa. The whole device was subjected to a 10 m/s^2 acceleration along Z axis.

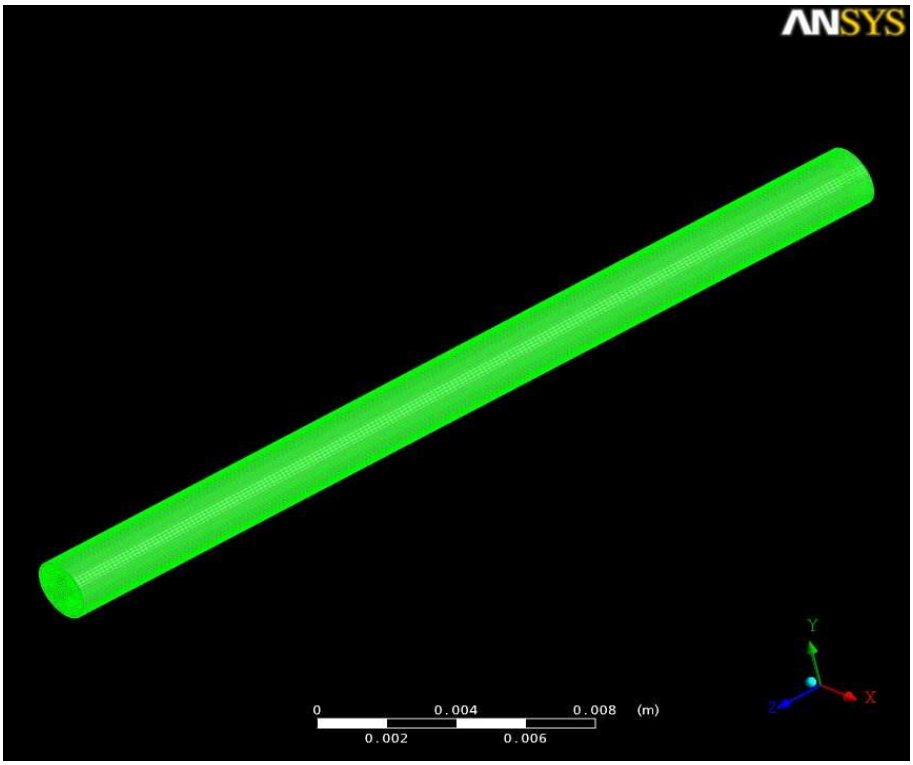

Figure 4.1: The CFX Model of Circular Tube

4.2 Transient Model Results

After the simulation was done, the results were displayed for investigation. Figure 4.2 is the mercury movement trace in the duct. From the figure, it was noticed that the

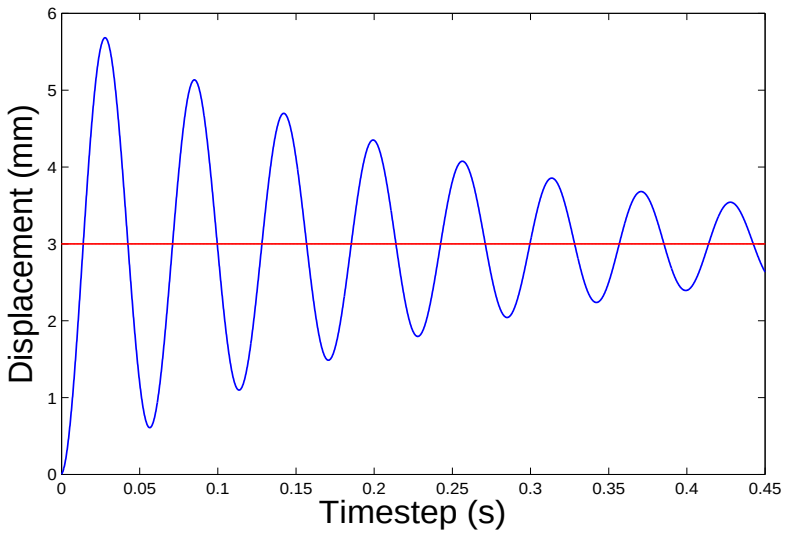

Figure 4.2: Movement of Mercury In Duct

mercury movement has not ceased completely by the end of the simulation. That is because it was very complicated simulation based on our facility. The simulation only proceeded 2400 timesteps (0.0001 s/timestep) , took 80G space in hard drive and 240 hours to complete. Even though, it is clear enough to confirm our assumption. From the displayed results, we can see by the accelerated force, mercury moved along the channel in duct as a cohesive blob all the time. Due to air pressure, mercury oscillated back and forth and tended to come to equilibrium at 3mm, meaning that final displacement was 3mm. We compare this with the analytical prediction of Equation 3.10:

$$C = \frac{13534kg/m^3 \times 10 \times 10^{-3}m \times 10m/s^2}{2000Pa} = 0.663 \tag{4.1}$$

Therefore,

$$x = \frac{10 \times 10^{-3} m(\sqrt{1+C^2}-1)}{C} = 3.0145mm \tag{4.2}$$

It has a perfect match between simulation and analytical result, strengthening the assumption of our theory and possibility of our design. Another observation is that the damped oscillation takes a relative long time to reach equilibrium. In this scenario, the response time should be counted as the time it takes the drop to reach its maximum displacement. The whole mercury movement was recorded and made into a video. Figure 4.3 are some pictures cut from the video.

4.3 ANSYS CFX Steady-State Analysis

Another simulation by ANSYS CFX is to analyze the steady-state flow. In the transient analysis, CFX has shown that the design of fluid droplet in tube is feasible under certain circumstance. So in steady-state analysis, we are going to explore the possibility of fluid droplet in different tube shapes and sizes. The reasons for performing steady-state analysis are below:

• we need to know how the fluid is going to behave in different tube shapes, such as circular and square tubes. Both shapes are capable of being fabricated by MEMS. So the steady-state results help decide what kind of shape is better for design.

• We need to know the tube size limitation for holding a fluid droplet as a blob. Even though a liquid with high contact angle and strong surface tension is selected, the fluid still cannot cohere if tube size is over a certain limit. The steady-state model will predict that limit.

• Steady-state analysis will allow us to estimate how response time varies when we change the device dimensions or the working fluid.

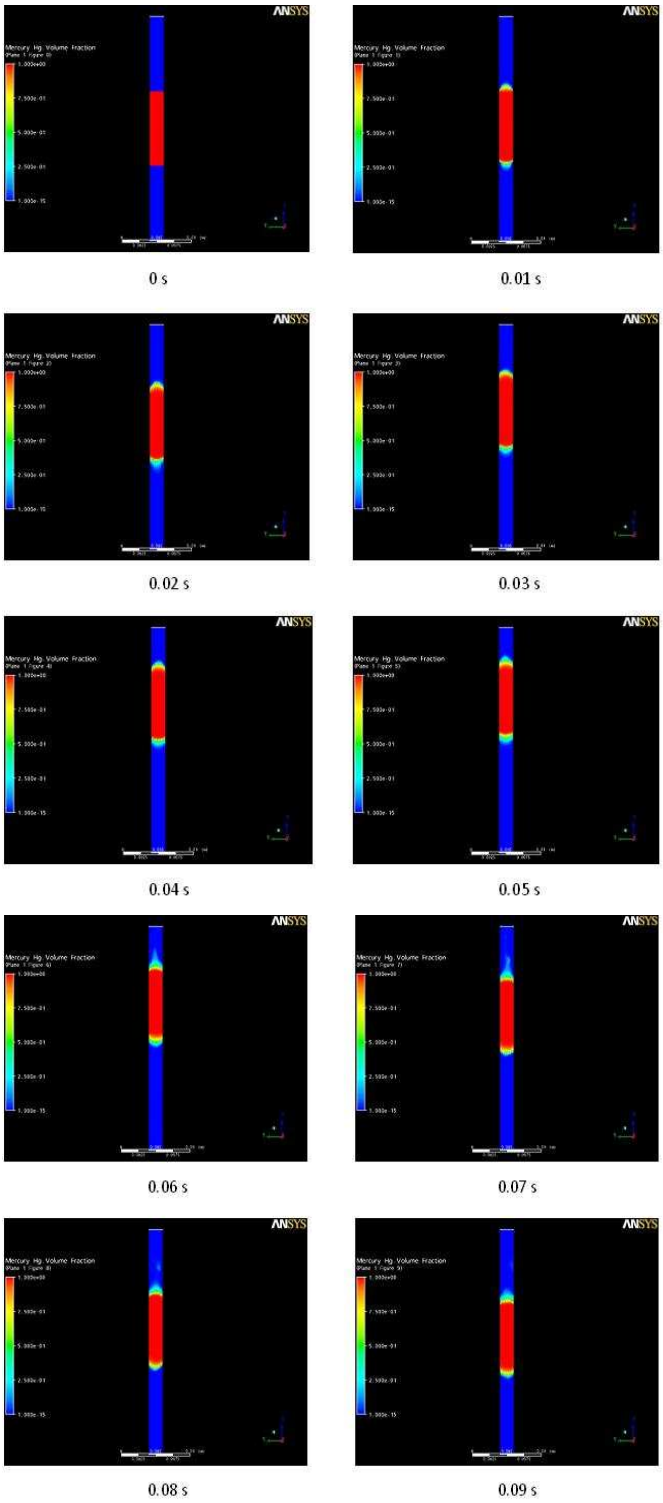

Figure 4.3: Mercury's Oscillation In Duct

4.3.1 Parameter Settings

In steady-state models, the flow of mercury through 30-mm-long open-ended tube was modeled at several velocities, and graphs of flow rate versus pressure drop were generated. The response time would be calculated from fluid displacement and its velocity. Although this response time is not exact value when fluid moves in airtight tubes, it is proportional to the real value. So it can help analyze what kind of sizes or shapes is better for design.

For circular tubes, we built $1.5mm$, $2mm$, $4mm$, and $5mm$ as diameters. For square ones, there are $1 \times 1mm^2$, $2 \times 2mm^2$, $3 \times 3mm^2$, and $5 \times 5mm^2$. The velocity was input from 0.2 m/s to 2.0 m/s in each size and shape. The flow movement is laminar without any turbulence.

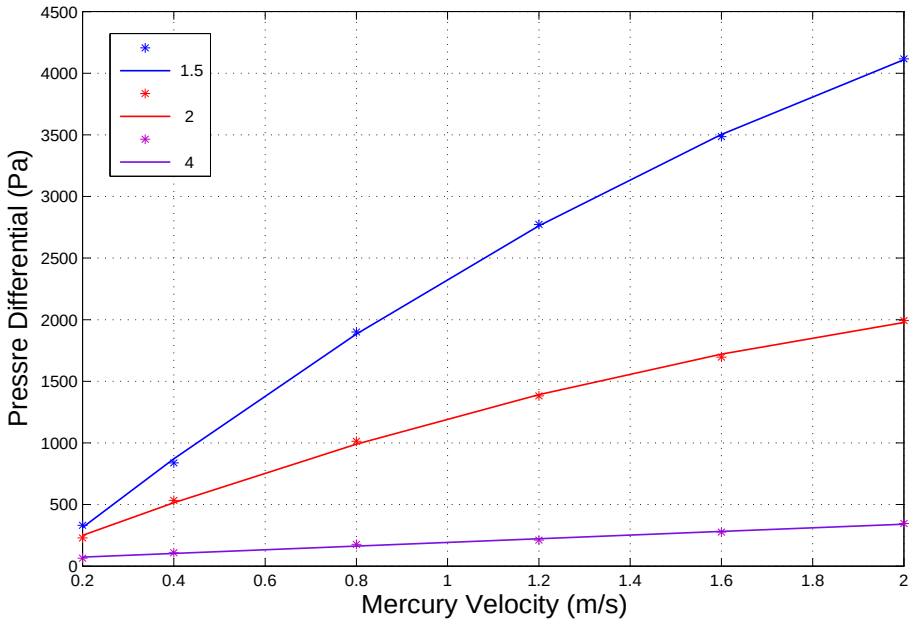

Figure 4.4: Circular Tube Pressure Differential vs Velocity

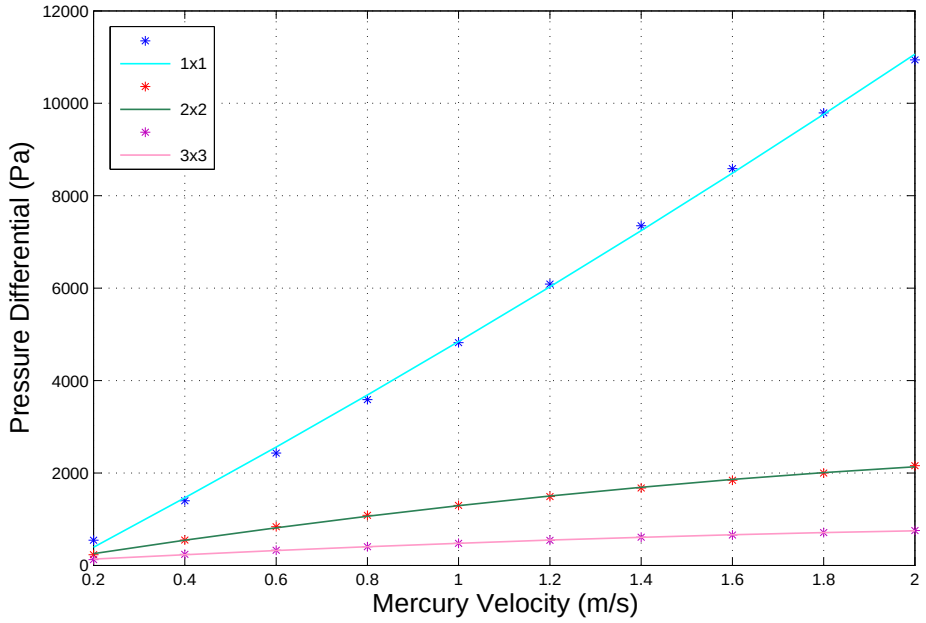

Figure 4.5: Square Tube Pressure Differential vs Velocity

4.3.2 CFX Steady-State Analysis vs Theoretical Calculation

CFX simulation results have given us encouraging predictions. However, how reliable are CFX results? Can we use CFX results to be the foundation for our design? In order to test this, comparison between CFX results and theoretical calculations is necessary. In chapter 3, we have found Poiseuille's and Bahrami's equations (Eq. 3.13 - Eq. 3.18) for laminar-flow fluid in circular and square ducts. CFX results will be compared with theoretical calculations to show their relationship.

An additional factor that needs to be considered is the entry loss – there is a pressure loss connected with going from plug flow on entry to the fully-developed laminar flow profile further down the tube, and this pressure loss is given by a factor of the form:

$$\Delta p = \frac{k \cdot \rho \cdot v^2}{2} \tag{4.3}$$

where ρ is the fluid density, v is the mean fluid velocity in the pipe, and k is a constant determined by geometry usually in the range 0.1-1. The entry loss is negligible for low flow rates, but becomes increasingly large as flow rate goes up and as fluid density goes up. This entry loss needs to be added into theoretical calculation, because the CFX simulation is of a short pipe (3 mm), and the entry losses become significant. So the total theoretical pressure drop, plotted as a continuous fluid in the following graphs, is given by:

$$\Delta p(total) = \Delta p(Poiseuille/Bahrami) + \Delta p(entryloss) \tag{4.4}$$

Fig. 4.6 - Fig. 4.9 are plotted to illustrate their results' agreements in each size and shape tube. These graphs show that we are able to obtain realistic results from CFX, so we can trust the CFX movie of the accelerometer. They show that we can also trust the Bahrami formula, so we can rely on it for our calculations of response time.

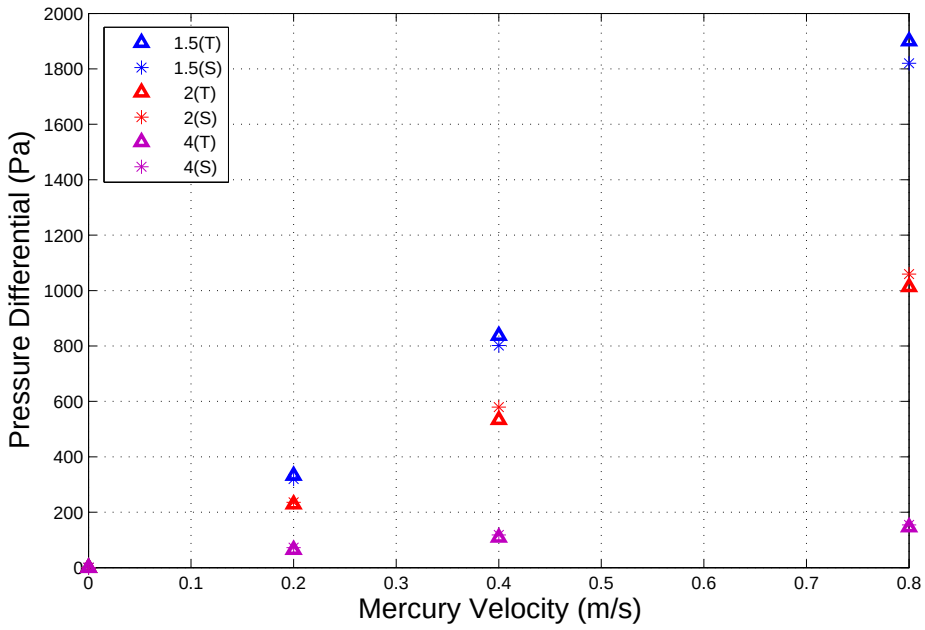

Figure 4.6: Mercury Theoretical Calculation vs CFX Result in Circular Tubes

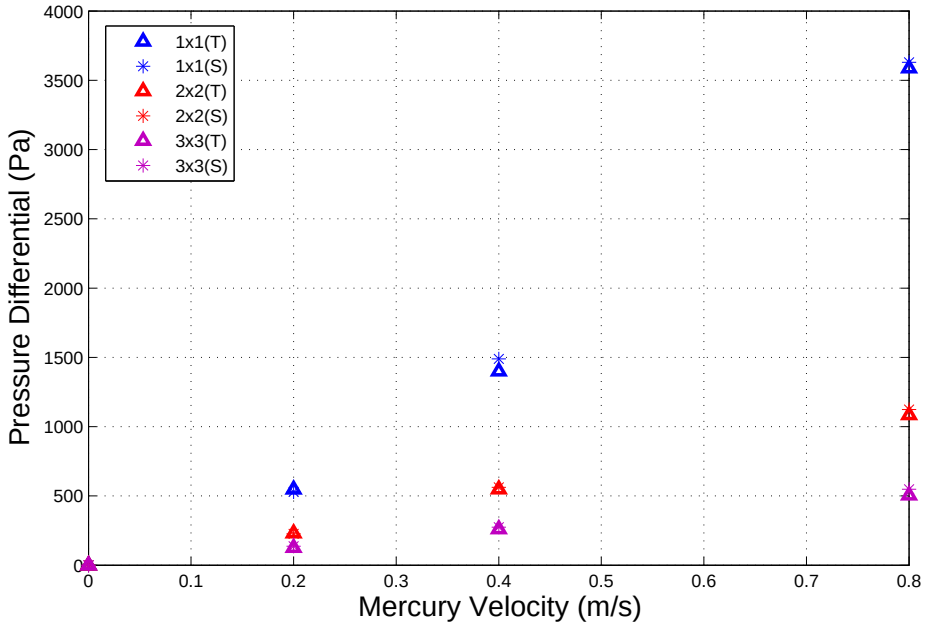

Figure 4.7: Mercury Theoretical Calculation vs CFX Result in Square Tubes

4.4 Steady-State Model Result

Figure 4.10 and 4.13 illustrate fluid velocity and pressure changes during simulation. From pressure changes figures, inlet pressure is higher than outlet pressure, because of the pressure drop due to fluid friction. The velocity near the wall is slower than near the center, which makes sense due to friction between wall and fluid retarding velocity. For $5mm$ round tube and $5 \times 5mm^2$ square one, CFX shows that they can not be simulated, because in neither of them mercury can hold together a blob when moving.

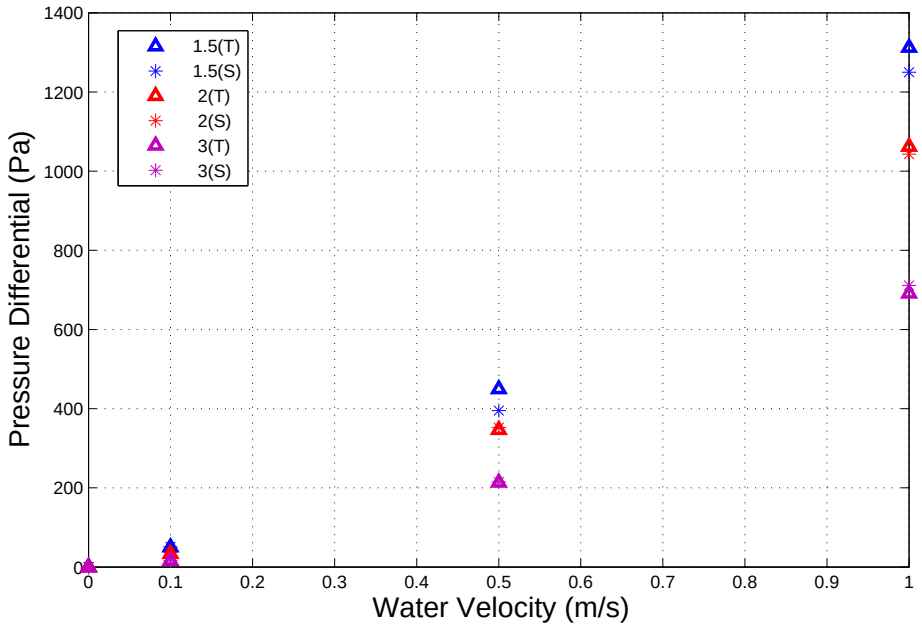

Figure 4.8: Water Theoretical Calculation vs CFX Result in Circular Tubes

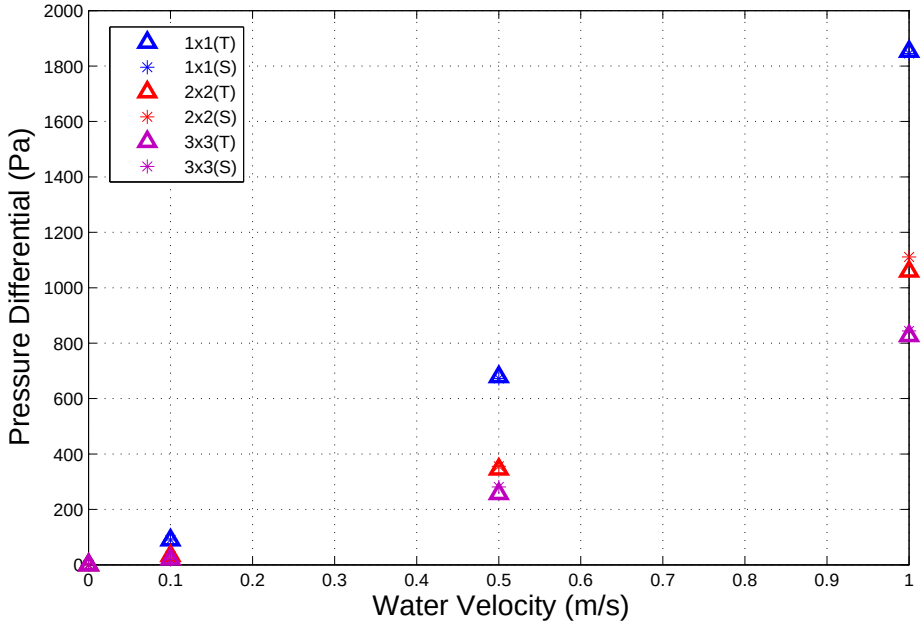

Figure 4.9: Water Theoretical Calculation vs CFX Result in Square Tubes

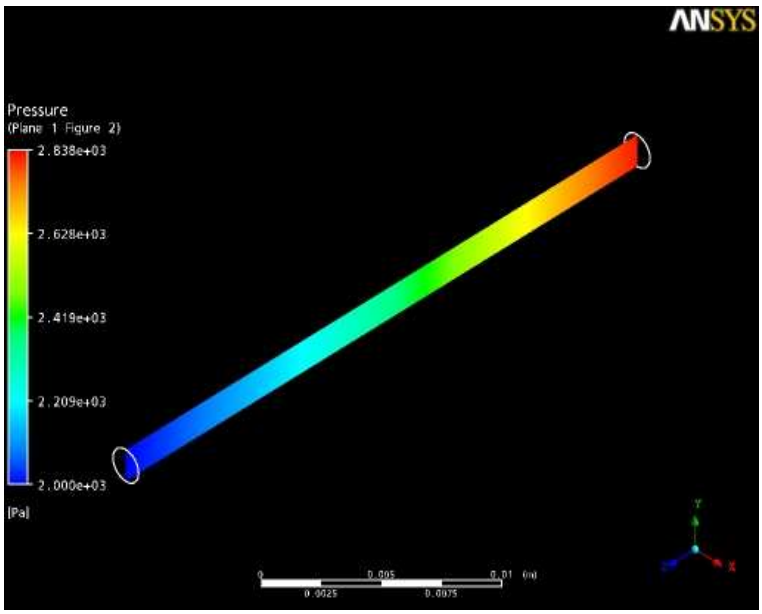

Figure 4.10: Pressure Changes in A Circular Tube

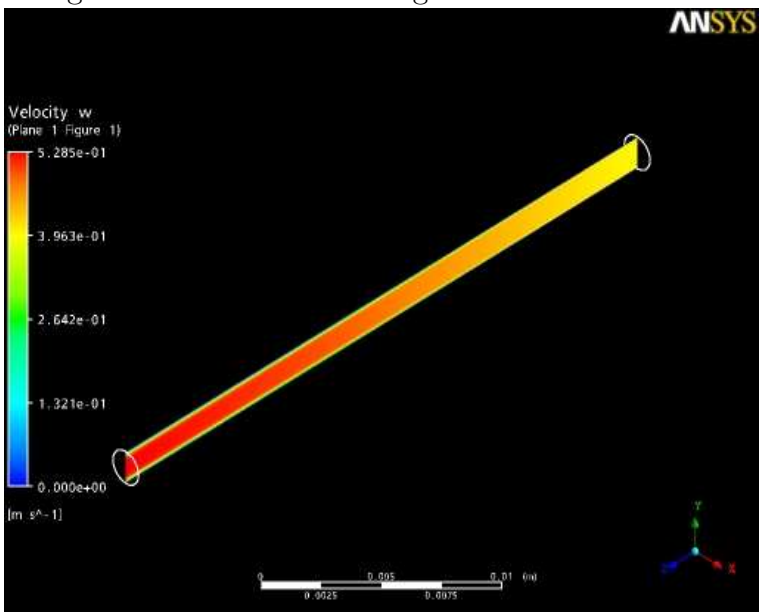

Figure 4.11: Velocity Changes in A Circular Tube

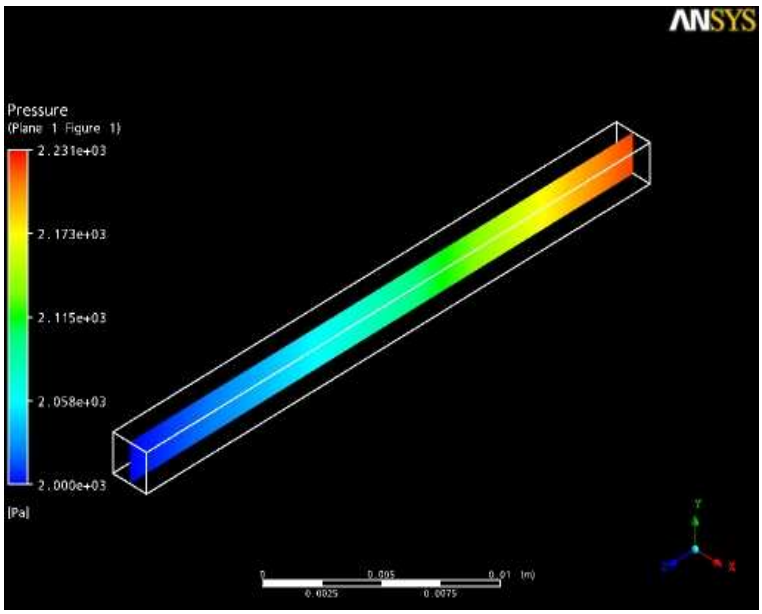

Figure 4.12: Pressure Changes in A Square Tube

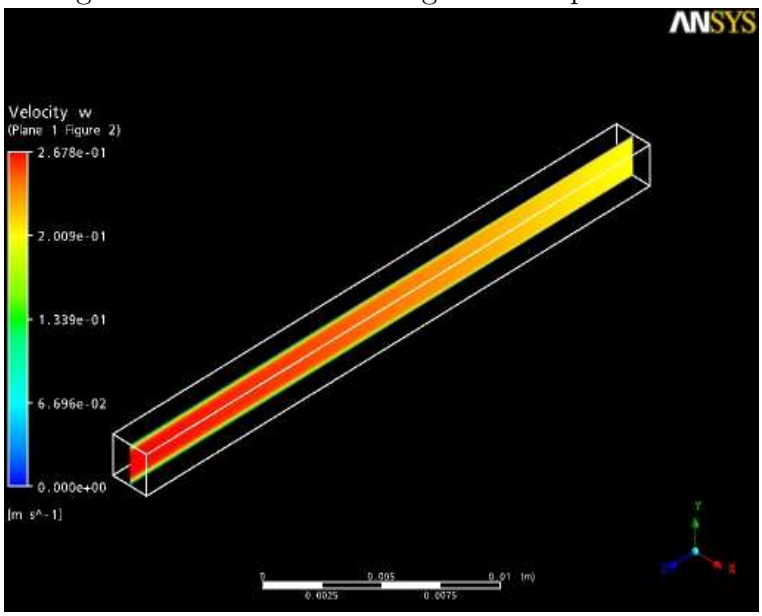

Figure 4.13: Velocity Changes in A Square Tube

4.5 Conclusion

In this chapter, the CFX model of liquid droplet with air cushions enclosed by a circular tube has been extended to model the transient following the application of an acceleration and the steady-state following the application of a velocity. The results of the transient modeling have been used to prove the feasibility of our liquid droplet design and the accuracy of our formula for sensitivity, and the steady-state modeling have been used to derive correlations between response time, fluid properties and device geometry. The calculations derived in this chapter confirm Poiseuille and Bahrami equations for fluid flow rates, and these equations can now be used in Chapter 6 to predict the effect of the choice of working fluid on response time.

Chapter 5

Experimental Studies

In this chapter several sizes and shapes of tube were tested to verify the numerical simulation results, and several resistive and capacitive test rigs were built and tested.

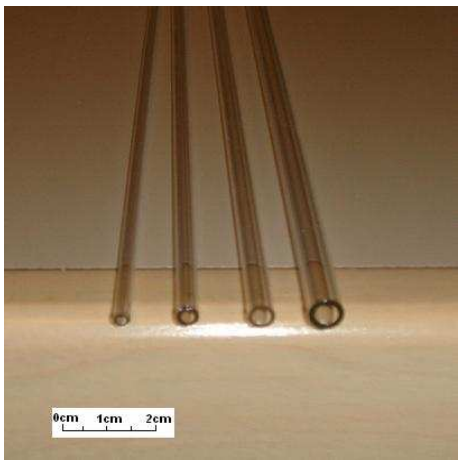

Figure 5.1: Circular Tubes

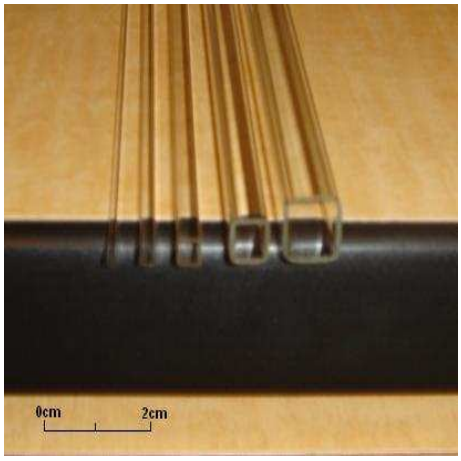

Figure 5.2: Square Tubes

5.1 Steady Flow Experiments

5.1.1 Mercury Steady-Flow Experiments

The primary factors affecting the liquids' performance have been explored. In numerical analysis, the steady-state results of liquid droplet moving in open tubes were simulated in different shapes and sizes. The following experiments were performed to verify them: test the performance of the same amount of liquid in different dimensional tubes of both circular and square cross-section. Four different diameters for circular tubes: $1.5mm$, $2mm$, $4mm$, $5mm$ and 4 different sizes square of tube: 1 x $1mm^2$, 2 x $2mm^2$, 3 x $3mm^2$, 5 x $5mm^2$ (shown in Figure 5.1 and 5.2), every tube in experiments contained the same amount of mercury, and was tilted at four individual angles: $30°, 45°, 60°, 90°$. In the first three angles, travel time from beginning spot to the bottom of the tube was recorded by stop watch. For tilted 90° angle,the distance that mercury moved down in the airtight vertically-placed tube was measured.

Figure 5.3: Experiments of Mercury in Open Tube

The setting of experiments are shown as in Fig 5.3. First of all, the white cardboard

Table 5.1: Mercury Movements in Circular Tubes

Diameter mm	Travel Distance	Travel Time s			Displacement at 90° (mm)
		30°	45°	60°	
1.5	140 mm	0.4	0.3	0.2	1.5
2	115 mm	0.3	0.25	0.18	0.7
4	130 mm	0.32	0.23	0.2	0.3
5	N/A	N/A	N/A	N/A	N/A

Table 5.2: Mercury Movements in Square Tubes

Square Tube mm	Travel Distance	Travel Time s			Displacement at 90° (mm)
		30°	45°	60°	
1 x 1	169 mm	0.5	0.35	0.3	5
2 x 2	154 mm	0.4	0.3	0.2	1.5
3 x 3	152 mm	0.4	0.3	0.2	0.7
5 x 5	N/A	N/A	N/A	N/A	N/A

where $30°, 45°, 60°, 90°$ have been marked was vertically standing behind for reference as well as a stopwatch on the side for timing. For each time, a certain amount of mercury was injected into the tube to keep the lengths of mercury droplet the same, and the tube was tilted as exactly same angle as the ones marked on board for consistence and accuracy. On the tube, there is a mark to ensure the distance that fluids travel the same. The whole procedures were shot by video. Through the video, the travel time can be computed by counting the time.

From the table it is concluded that circular tubes with diameter lower than 4mm, and square tubes with cross-section smaller than 3 x 3 mm are able to hold mercury together as a blob.

For the sealed tubes placed at 90° angle, mercury displacement was measured, which also can be calculated using Equation 3.8 and 3.10, shown in Table 5.3. Experimental

Table 5.3: Mercury Displacement Comparison

Square Tube	Experimental (mm)	Theoretical (mm)
1 x 1	5	4.9
2 x 2	1.5	1.1
3 x 3	0.7	0.497
Round Tube	Experimental (mm)	Theoretical (mm)
1.5	1.5	1.37
2	0.7	0.64
4	0.3	0.179

and theoretical results agree well.

The following figures give experimental results for velocity/pressure drop versus tube diameter squared or cross-section area. The pressure drop in each case is taken to be the hydrostatic pressure exerted by the mercury droplet. Both numerical and experimental results has given matching results for square and circular tubes.

5.1.2 Water Steady-Flow Experiments

Mercury steady-flow experiments tell us that the results from experiments and simulations are matching each other. How well these results match with Equation 3.13 - 3.17 is another question to be resolved by a new set of experiments. Fig 5.6 illustrates an experimental configuration where a funnel interconnects with a glass tube (L mm in length), while water from tap is filled into the funnel and a measuring cup collects water that runs out from the glass tube. For each shape and size tube, when water level in the funnel is at certain heights (h mm), we time a certain volume of water (V mL) flowing through the glass tube are gathered by the measuring cup. Therefore:

$$Q = \frac{V}{t} \tag{5.1}$$

$$u = \frac{Q}{A} \tag{5.2}$$

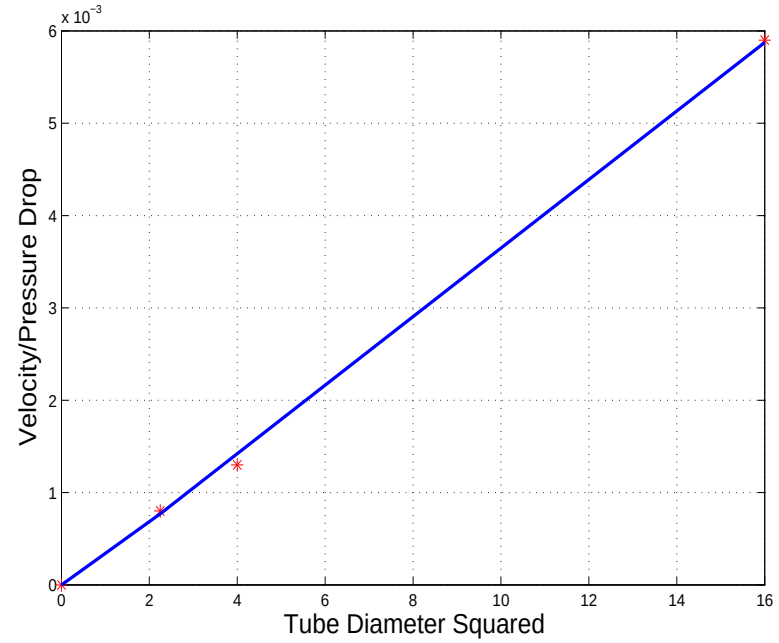

Figure 5.4: Velocity/Pressure Drop vs Tube Diameter Squared (Mercury)

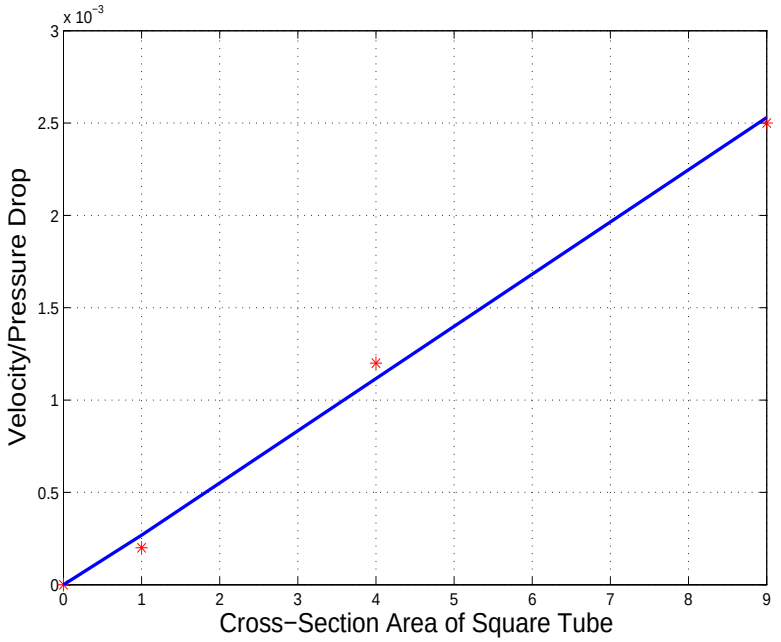

Figure 5.5: Velocity/Pressure Drop vs Square Tube Cross Section (Mercury)

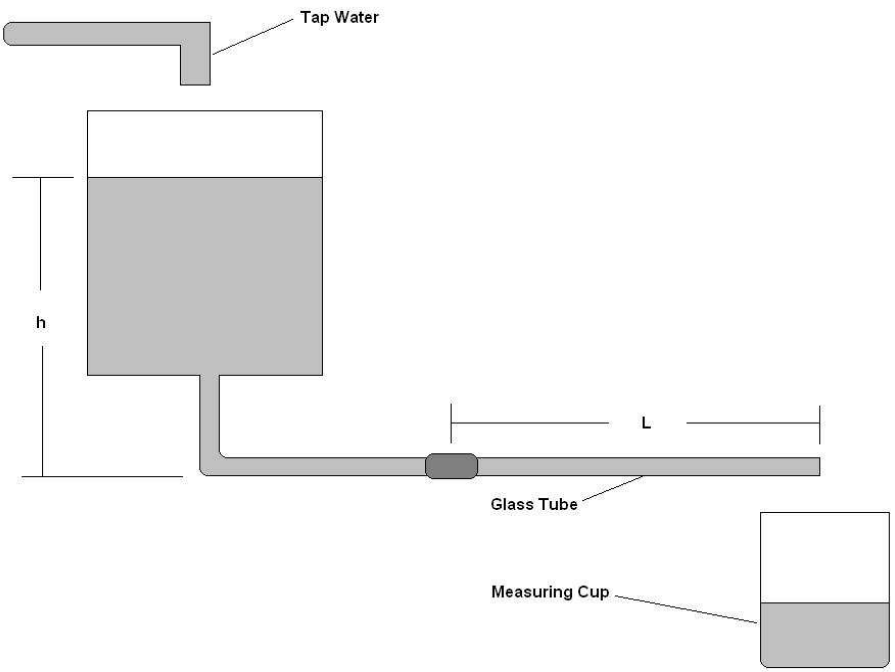

Figure 5.6: Steady Flow Experiment Configuration of Water

Where:
Q: the volume flow rate
A: the cross section area
u: the velocity of flow

According to Equation 3.13 - 3.17, the velocity can be obtained for round and square tubes respectively:

$$u = \frac{\Delta p d^2}{32 \mu L} \tag{5.3}$$

$$u = \frac{\Delta p c^2}{\mu L}\left(\frac{1}{3} - \frac{64}{\pi^5}\tanh(\pi/2)\right) \tag{5.4}$$

Where:
Δp: is equal to $\rho \cdot g \cdot h$

Contrasting velocities in both experiment and theory, Fig 5.7 and 5.8 shows their comparison. The results confirm the agreement between steady flow experiments and equations, giving confidence that we can use the Poiseuille and Bahrami Equations to calculate response times.

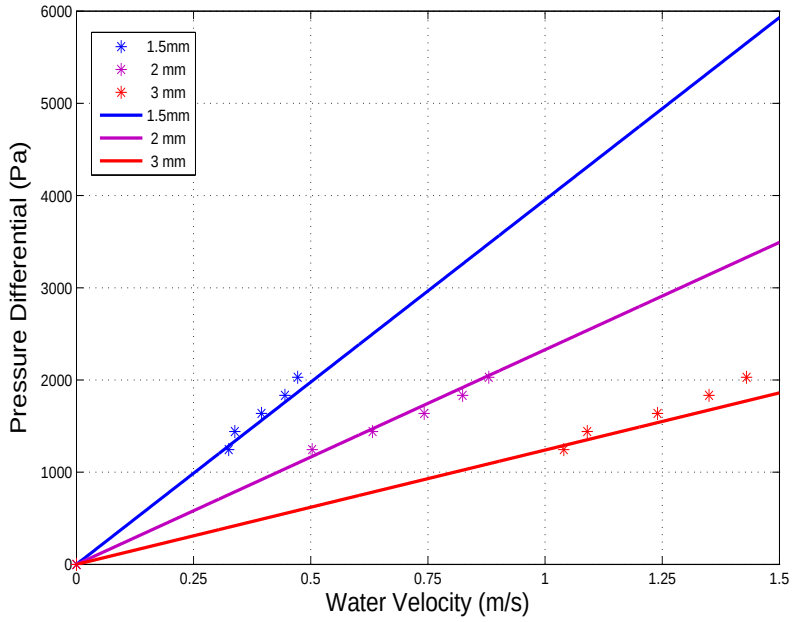

Figure 5.7: Circular Tube Experimental Pressure Drop vs Velocity (Water)

5.2 Construction of Liquid Droplet Accelerometer

5.2.1 Test Rigs of Liquid-Droplet Accelerometer

In the previous chapters, the design principles of the liquid droplet accelerometer were presented. The applied acceleration can be measured by several ways through

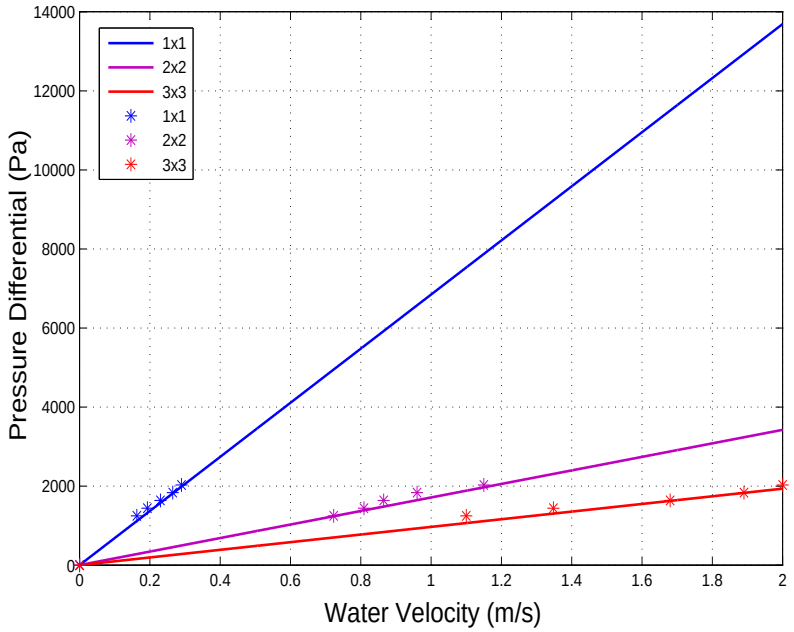

Figure 5.8: Square Tube Experimental Pressure Drop vs Velocity (Water)

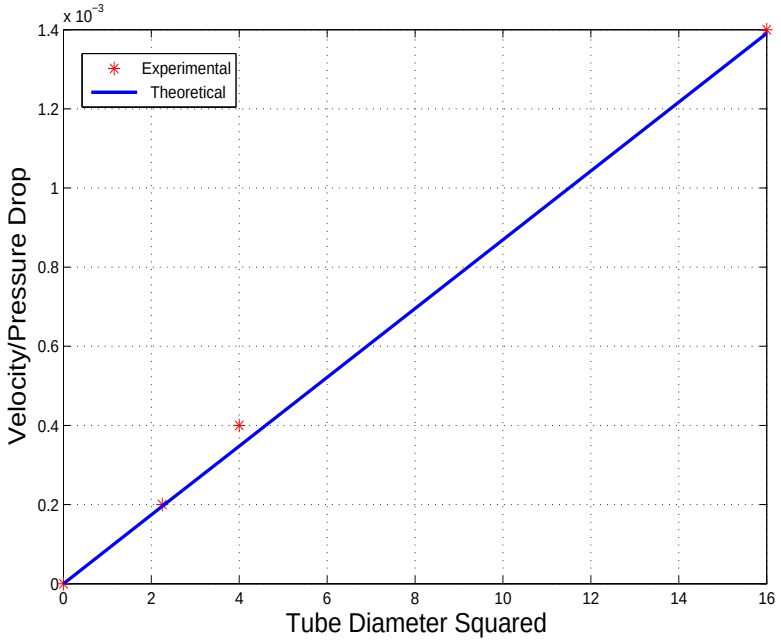

Figure 5.9: Velocity/Pressure Drop vs Tube Diameter Squared (Water)

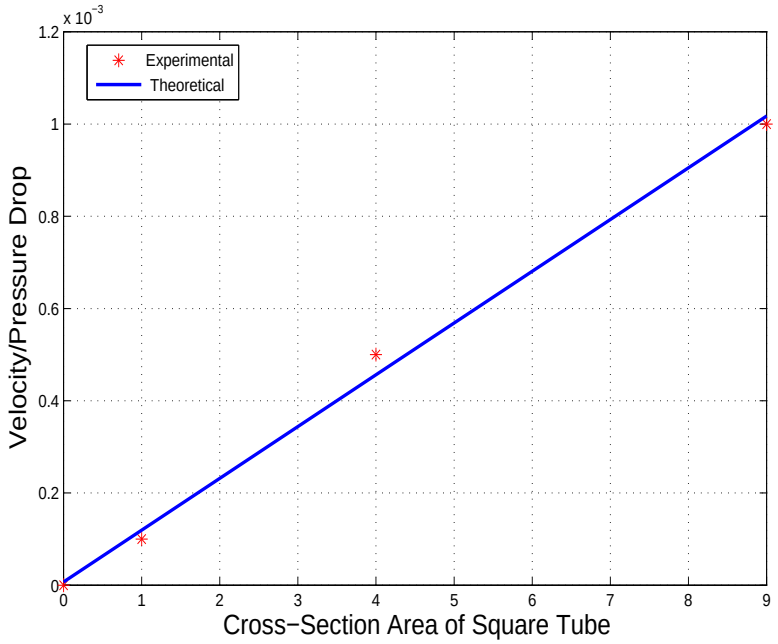

Figure 5.10: Velocity/Pressure Drop vs Square Tube Cross Section (Water)

detecting the distance that the droplet moves. In chapter 3, through theoretical analysis the moving distance is shown to be determined by the density of working fluid and the initial pressure of air cushion. But several practical questions must still be resolved before we can conclude that the accelerometer will work.

5.2.2 Operation of Resistive Test Rig

In Figure 5.11, Resistance Accelerometer Test Rig, a glass tube containing two parallel graphite conductors was sealed at one end. When the designated liquid moves in the tube and immerses both leads, a resistance difference should appear. Depending on how deeply the leads are immersed, the resistance value should allow us to calculate the distance the droplet has moved.

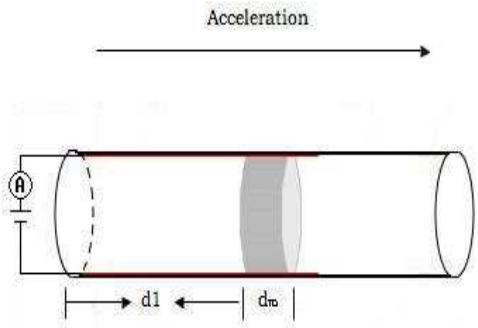

Figure 5.11: Schematic Design of Resistance Accelerometer

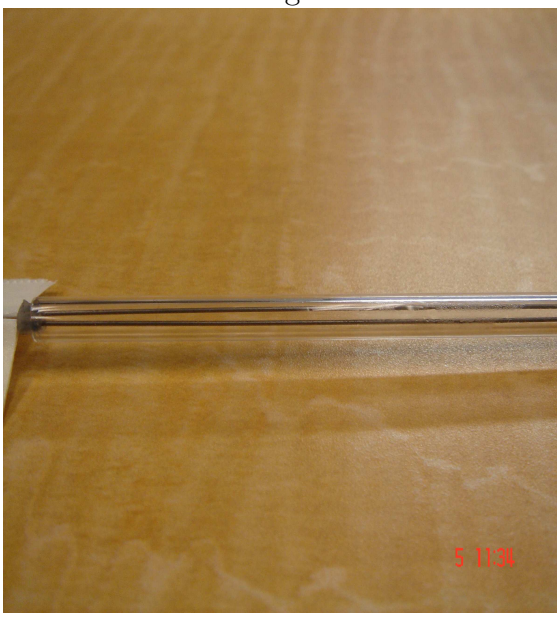

Figure 5.12: The Test Rig of Resistance Accelerometer

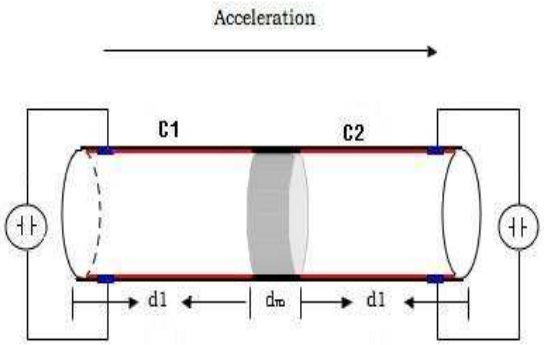

Figure 5.13: Schematic Design of Capacitance Accelerometer

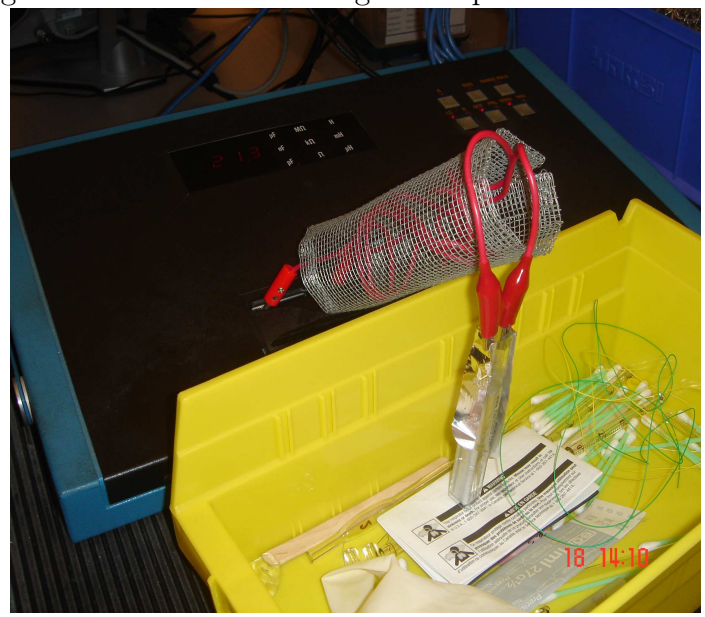

Figure 5.14: The Test Rig of Capacitance Accelerometer

5.2.3 Resistive Measurement Verification

The most important question for resistive measurement is how resistance changes when mercury moves along conductors only for few millimeters. If there is a large and variable contact resistance compared with the resistance of a few millimeters of conductor material, the design can not provide reliable results.

An experiment is set up to investigate how the circuit resistance changes when the graphite conductors are immersed in an increasing depth of mercury. So two nichrome wires were connected to two isolated graphite rods. A resistance meter was connected to these wires. At the beginning, mercury did not contact both rods and the resistance was infinite as shown on the meter. As the two graphite rods started submerging into mercury, the exposed length of graphite beyond mercury was shortened, so the conduction path through the graphite became shorter and shorter.

For the convenience of collecting data, graphite rods were marked by 8 scales, from $10mm$ to $80mm$. The resistance was measured as graphite was dipped in every $10mm$. The resistant values versus the depth of immersion were plotted into Figure 5.15.

Comparing resistance with the length of graphite immersed, it was found that the resistance fell linearly as the exposed length of graphite. Measured by Resistance Meter, each $90mm$ in length, $0.5mm$ in diameter graphite lead has 102.6Ω resistance, therefore its resistivity is given:

$$\rho = \frac{R \cdot A}{L} = 223.725 n\Omega \cdot m \tag{5.5}$$

At 25° mercury resistance is $0.984 n\Omega \cdot m$, that could be neglected by comparison with the resistance of the rods. In theoretical analysis the graphite resistance decrease versus immersion of mercury is also shown in Figure 5.15. Comparing both resistance changes, it can be seen that the resistance fell linearly as the exposed length of graphite, which was very similar to analytical results. Hence experiment study

confirms that stable signal output can be achieved and the resistance change is linear; there is not a significant contact resistance between the mercury and graphite that will vary unpredictably.

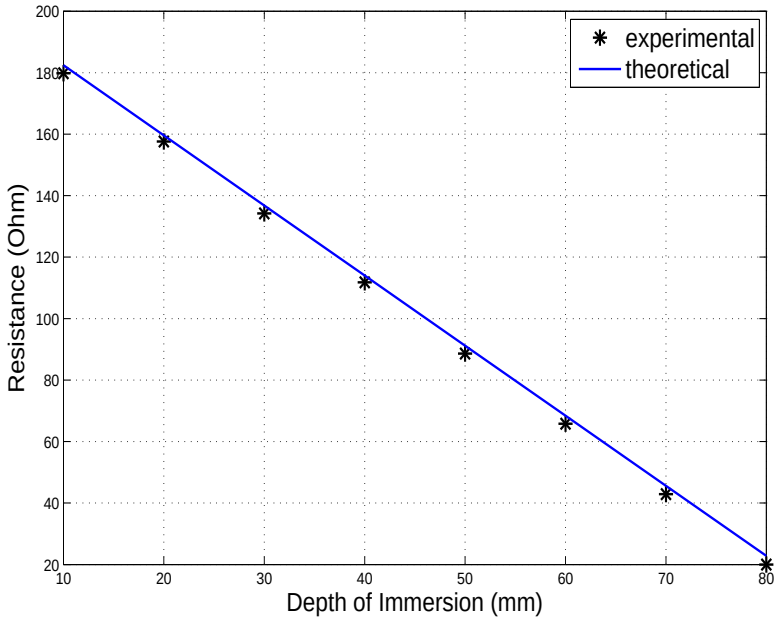

Figure 5.15: Circuit Resistance vs Depth of Immersion

In this experiment, it was also found that mercury as working fluid has a low enough resistivity to be neglected while our selected graphite has relative high resistivity. Hence, the absolute change of resistance only depended on the conductors. For those working fluids that have non-negligible resistivity (poor conductors), the signal collecting and processing would be more complicated, even leading to inaccuracy. Because that will depend on the relative conductivity of the fluid and conductors. The percentage change in resistance will be small if the fluid has a high resistance. In order to avoid this, when selecting working fluid for resistive model accelerometer, high conductivity must be considered as priority. Mercury with graphite in this experiment has been proven a suitable combination.

5.2.4 Operation of Capacitive Test Rig

The Figure 5.14 Capacitance Accelerometer test rig consists of a square duct and two strips of aluminium foil wrapped tightly along the inside wall. Aluminium foil was stuck onto the wall to prevent working fluid from flowing beneath the foil, wetting the walls. The liquid's movement in the tube, between the two aluminium foils is expected to cause capacitance value changes.

The dimension for each aluminium foil is $12mm \times 98mm$ and distance between foils is $12mm$. Silicone oil, a high dielectric insulating fluid, was selected as working fluid. The capacitive values were collected at every $25mm$ increase in the level of silicone oil in the tube. Theoretical calculation for this capacitance, it shows:

Before the tube is filled with silicone oil, according to:

$$C = \frac{\epsilon_0 \cdot A}{d} \tag{5.6}$$

Where:
$\epsilon_0 = 8.854 \times 10^{-12} F/m$
$A = 0.012 \times 0.098 = 11.76 \times 10^{-4} m^2$
$d = 0.012m$
Thus:

$$C = \frac{8.854 \times 10^{-12} \times 11.76 \times 10^{-4}}{12 \times 10^{-3}} = 0.8677 \times 10^{-12} F = 0.8677pF \tag{5.7}$$

After silicone oil was full-filled into:

$$C_r = \epsilon_r \cdot \frac{\epsilon_0 \cdot A}{d} \tag{5.8}$$

Where:
$\epsilon_r = 2.9$
Thus:

$$C_r = 2.9 \times \frac{8.854 \times 10^{-12} \times 11.76 \times 10^{-4}}{12 \times 10^{-3}} = 2.516pF \tag{5.9}$$

According to Equation 2.8, when silicone oil was filled a quarter, two quarters and three quarters high of tube, the capacitance will be these values respectively:

$$\begin{aligned} C_{0.25} &= 0.75 \times C + 0.25 \times C_r = 1.28pF \\ C_{0.5} &= 0.5 \times C + 0.5 \times C_r = 1.69pF \\ C_{0.75} &= 0.25 \times C + 0.75 \times C_r = 2.10pF \end{aligned} \tag{5.10}$$

The following graph displays the capacitance corresponding to the depth of immer-

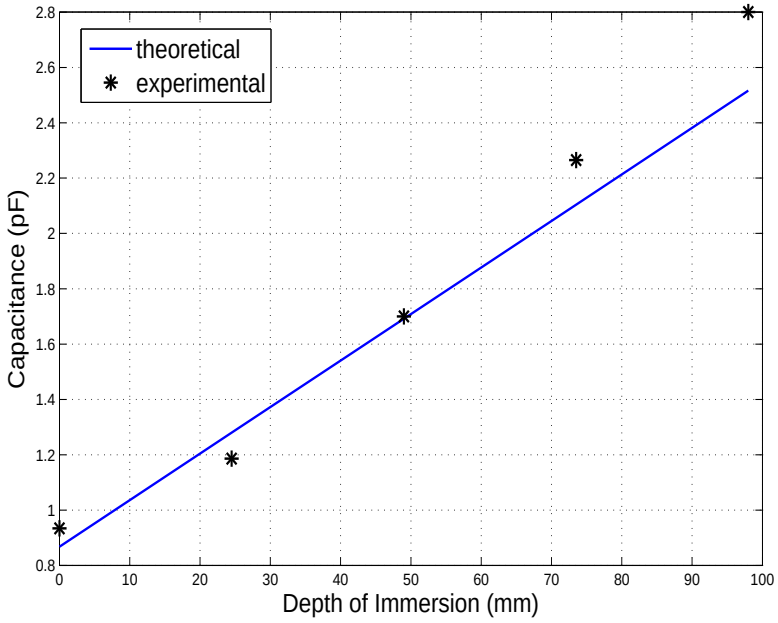

Figure 5.16: Capacitance vs Depth of Immersion

sion of silicone oil from experiments and theoretical analysis. It is realized that the capacitance found from experiments was higher than the calculated capacitance. The simplicity of equipments, insufficiency of shield as well as the extreme small value would cause inaccurate numbers, which is difficult to eliminate based on our facilities.

Nonetheless, we are happy to see that the capacitance was increased almost linearly.

From this experimental and theoretical comparison, it was verified that we can detect fluid motion by this method, and that we can measure capacitance changes in the pico-Farad range. Because of the small signal output, a good shielding protect for this device is important. If necessary, an output amplifier will be mounted for enhancement of signal, which will be discussed in future work.

5.3 Conclusion

In this chapter, we have carried out the experimental work as a supplement to theoretical and numerical study of steady-state and transient cases. We initially performed a steady-state flow experiment, measuring velocity and pressure drop, to prove that both experimental and theoretical results coincided and to validate the flow-rate formulas that will be used to calculated response time. Then, both resistive and capacitive test rigs were built for further tests to eliminate concerns of both designs. The results have shown so far that both designs are feasible, providing a basis for identification of a more suitable working fluid and material combination to improve both sensitivity and response time as well as provide practical fabrication process.

Chapter 6

Choice of Materials and Fabrication Process

6.1 Choice of Working Fluid

Choosing the most suitable liquid is key towards our success. A list of requirements is necessary to evaluate all liquids, such as conductivity, permittivity, etc. In the experiments, the glass tube, aluminium foil and grease proof paper have been considered as wall materials being tested together with liquids.

6.1.1 DI Water

Deionized water, also known as DI water, is purified water that does not contain mineral ions such as cation and anions. DI water, as one kind of liquid droplet, has its advantages to be considered into design. It has high resistivity. DI water has up to $1.83G\Omega \cdot m$ resistivity compared with tap water (around $1.5M\Omega \cdot m$), which is not convenient for resistivity measurement. DI water also has a high dielectric constant number, which is 80.4 at 20°C. If adopting capacity measurement, DI water is able to increase 80 times higher capacitance theoretically. From fabrication and environmental consideration, DI water is non-toxic and available.

However, DI water has a few drawbacks, that a set of experiments has confirmed. The surface tension of DI water is too small to form over 90 degree contact angle with most potential duct materials. It usually wets the duct. After we injected DI water into glass tube and moved the tube, DI water left a long trace while the bead of DI water itself lost volume.

If testing DI water on aluminum and grease proof paper, the phenomenon of long trace becomes less significant, yet still influence the application negatively. The only surface on which DI water performs well is Teflon. Freezing point is another concern when ambient temperature goes down to 0 degree, which could damage the accelerometer device as a result of the working fluid turning into solid and expanding its volume.

6.1.2 Methanol

Methanol, the simplest alcohol, was chosen for experiments, because it is a common chemical compound with 32.6 dielectric constant at 20°C.

From the experiments, methanol was found to wet the glass tube. The volatility of methanol is also a serious defect in this design since its vapor pressure sets a lower bound to the working pressure of the device. It is also a poisonous liquid, unhealthy for human beings, which is the reason methanol would not be used for current research.

6.1.3 Silicone Oil

Silicone Oil, due to its being environment friendly, was selected for testing. It is also a perfect liquid for electrical insulating. When moving along in the glass tube, it displayed its high viscosity as a disadvantage. Compared with other liquids that have been tested, it has high viscosity value, and therefore its response time will be unacceptably long.

Table 6.1: Properties Comparison Between Mercury And Galinstan

	Mercury	Galinstan
Boiling Point (°C)	356.73	1300
Freezing Point (°C)	-38.83	-19
Density g/cm^3	13.534	6.44
Viscosity $mPa \cdot s$	1.526	2.4
Resistivity $n\Omega \cdot m$	961	435

6.1.4 Mercury

Mercury, a liquid metal, has high conductivity and low resistivity, and is therefore a primary candidate in the resistive design. In section 4.1.1 it was already observed how smoothly mercury moves along the tube. In chapter 3, mercury is also chosen to be in the simulation, and it turns out that the results are very satisfying. However, mercury has the major drawback that it is toxic.

6.1.5 Galinstan

Galinstan is an eutectic alloy of gallium, indium, and tin which is liquid at room temperature. Nowadays, galinstan is getting more attention as a non-toxic replacement for mercury. Because it was found that it has similar properties to mercury. Table 6.1 shows the comparison of physical properties between mercury and galinstan.

Although Galinstan is a similar liquid to mercury it is safe, non-toxic and environmental friendly. Therefore, it is another good selection for droplet accelerometer. However, galinstan tends to wet and adhere to many materials, including glass. If it is employed, the inner tube must be coated with gallium oxide to prevent the alloy from wetting the surface. This coating process is a very common technology with low cost, and is used to manufacture galinstan-based clinical thermometer.

Table 6.2: Fluid Sensitivity Comparison at 2 KPa

Liquids	Density Kg/m^3	Distance mm
Galinstan	$6,449$	1.58
Mercury	$13,579$	3.02
Methanol	791.8	0.19
DI Water	997.05	0.24
Silicone Oil	920	0.23

Table 6.3: Fluid Sensitivity Comparison at $20°C$ Vapor Pressure

Liquids	Density Kg/m^3	Vapor Pressure Pa	Distance mm
Galinstan	$6,449$	< 0.16	> 9.975
Mercury	$13,579$	0.16	9.998
Methanol	791.8	$12,977.4$	0.030
DI Water	997.05	2338.468	0.208
Silicone Oil	920	0.00025	9.989

6.2 Sensitivity

One basis of comparison between fluids is the sensitivity, that is, the distance each fluid droplet moves under standard conditions. The further the droplet moves, the higher sensitivity it has. In Chapter 3 Equation 3.11 and 3.12 were derived for predicting displacement of every kind of liquid, and are used to estimate sensitivity. In our comparison, it is assumed that liquid drop is $10mm$ long and each air cushion is $10mm$ long. The first comparison of sensitivity (Table 6.2) is under a cushion pressure of 2000 Pa, and a second comparison (Table 6.3) is based on cushion pressure being equal to the vapor pressure of the candidate fluid at $20°C$.

Table 6.4: Fluid Response Time Comparison at 2 KPa

Liquids	Viscosity mPa·s	Velocity m/s	Response Time ms
Galinstan	2.4	1.953	0.809
Mercury	1.526	3.072	0.983
Methanol	0.59	7.945	0.024
DI Water	1	4.688	0.048
Silicone Oil	350	0.013	17

6.3 Response Time

Since we obtained moving distance for each liquid for comparing sensitivity, Equation 3.13 can be used to calculate the velocity for each liquid. Therefore, response time is the ratio between moving distance and velocity. Table 6.4 lists comparison of response time. It is seen that silicone oil, though in other respects a good candidate for the capacitive design, is ruled out by its high viscosity and consequent slow response.

6.4 Material Options for Inner Surface

Thomas Young's equation shows that in order to avoid fluids sticking to the walls a fluid with high surface tension, such as mercury, should be an important asset for this design. But other fluids can be used if a material is deposited on inner wall, creating a low-adhesion layer directly in contact with the fluid. Considering these materials for the duct walls will allow us to consider otherwise - unsuitable liquids.

6.4.1 Teflon

Polytetrafluoroethylene(PTFE) is a synthetic fluoropolymer which has a very low adhesion to water. PTFE is most well known by the DuPont brand name Teflon. Teflon is a white solid at room temperature, with a density of 2.29 g/cm^3 and melting point at 327°C. Its coefficient of friction is 0.1 or less, which is the second lowest of any

Table 6.5: Critical Surface Tension

Substrate Clean Smooth	Critical Surface Tension dynes/cm
Soda Glass	30
6063 Aluminum	45
301 Stainless	44
Teflon	18

known solid material, as well as it has excellent dielectric properties. Water, water-containing substances, or oil-containing substances, do not wet Teflon, as adhesion to Teflon surfaces is inhibited. Due to this property PTFE is used as a non-stick coating.

From Table 6.4 depicting Teflon's surface tension compared with others, Teflon is an ideal choice as deposited inner wall layer due to its low surface tension and high dielectric properties.

6.4.2 Gallium Oxide

As mentioned in previous section, Galinstan has similar properties to mercury except that Galinstan wets almost any material, which does not satisfy this design. To avoid this disadvantage, Gallium Oxide is adopted as a coating. It is a non-toxic, high melting point(1900°), metal oxide. Gallium Oxide strongly repels Galinstan, which is allowed to move smoothly on Gallium Oxide. This combination has been used in medical instruments such as thermometers patented by Geratherm Medical AG in Germany [28]. It resolves the problem of replacing mercury by a non-toxic fluid.

6.5 Choice of Materials for Designs

Since a few different materials have been looked into, the final step is to select an outstanding materials combination for each type of accelerometer. In either case, the elected fluid must not wet inner wall.

6.5.1 Choice of Materials for Resistive Accelerometer

For resistive accelerometer, we are expecting a conductive liquid as a droplet and a dielectric wall containing a pair of conductors exposed to the liquid.

Therefore, galinstan in a gallium Oxide deposited duct is an ideal choice. Our simulations and experiments have proved that mercury has suitable properties for resistive accelerometer except its toxicity. Galinstan is perfect to replace mercury, and has been widely used in medical areas throughout the world. The resistive conductors must be insoluble in galinstan. Therefore, graphite would be a suitable choice, since we have confirmed experimentally that it neither reacts with nor adheres to galinstan.

For a duct of the dimensions considered in Section 6.2, the sensitivity of galinstan is 1.9 $\mu V/g$ at 2000 Pa (if the power consumption is 10 mW), and response time is 0.809 ms for a 1-g acceleration.

6.5.2 Choice of Materials for Capacitive Accelerometer

For capacitive accelerometer, we are expecting a high dielectric liquid as a droplet and a pair of metal plates protected by an insulating layer from the droplet.

Therefore, DI water in a Teflon-coated duct is a possible choice, On Teflon, DI water has very low adhesion according to Thomas Young's equation, as well as having a high dielectric compared with air. The sensitivity of DI water would be 0.224 mm/g at 2000 Pa, and response time is 0.048 ms/g.

However, we see from Table 6.3 that it would be difficult to achieve this sensitivity in practice, as the vapor pressure of water at $20°C$ is already greater than 2000 Pa. And if the ambient temperature goes above $20°C$, the sensitivity will drop rapidly. So we do not have an ideal candidate for the capacitance design.

6.6 Fabrication Process

Since the experiments and simulations have been done, and a satisfactory design has been selected, now the general MEMS fabrication process can be discussed.

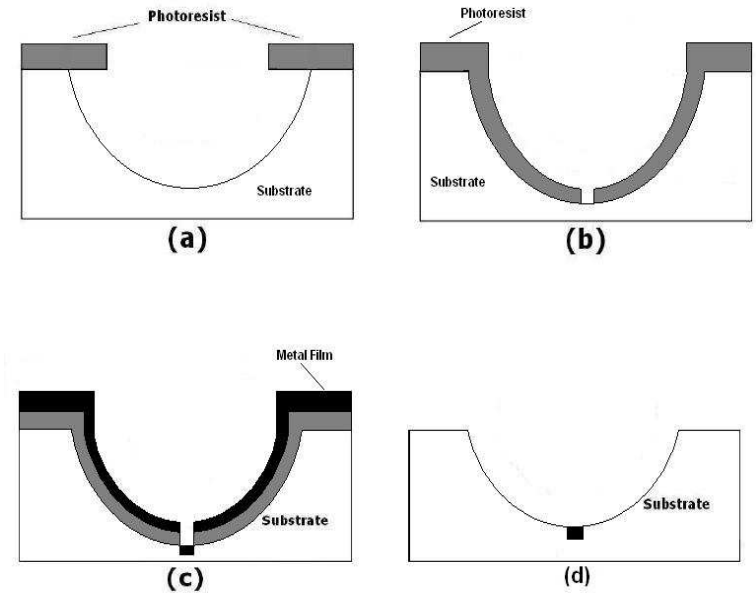

Figure 6.1: Fabrication Process of Circular Duct

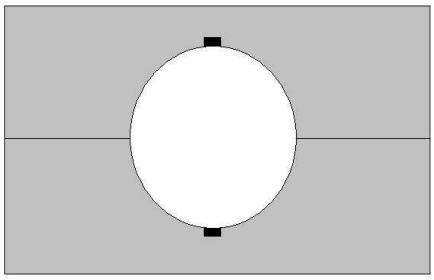

Figure 6.2: Cross Section of Accelerometer

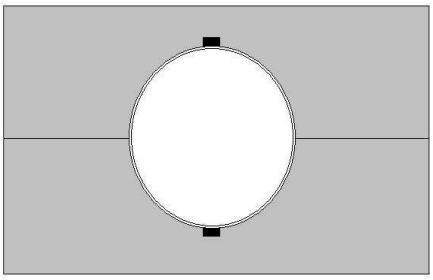

Figure 6.3: With An Insulating Layer

Considering the contact angle issue between mercury and inner wall surface, the ideal shape of micro-channel is a circular duct. First, a substrate wafer would be patterned

with photoresist and the exposed area will be etched using an isotropic etching solution with agitation to create the bottom semicircle, shown in (a) of Fig 6.1. After a second pattern, dry plasma etching can be adopted to etch a hole at the bottom (b), followed by spinning another photoresist on. In (c), a thin metal film should be deposited by evaporation on the top. After washing away the photoresist, the semicircle with a graphite strip at the bottom has been made, illustrated in (d). An electrically conductive liquid droplet is injected into the central position followed by the capping of the channel using a second semicircular top channel. Afterwards, the prototype is put in a vacuum chamber and sealed at a low pressure such as 100 Pa to increase the accelerometer sensitivity. Fig 6.2 shows the cross section of accelerometer.

Similar methods could be used for fabricating the capacitive version of the design. In this case, after process (d) deposit an thin insulating layer on the top, such as PECVD deposited Silicon Nitride, or Polyimide, Teflon. Therefore, the cross section would look like Fig 6.3.

If a square duct is adopted in the design, the fabrication differs from last one. The substrate wafer would be etched by dry plasma etching carving a rectangular hole. Next, dry plasma etching will etch a small hole at the bottom for depositing thin metal film by evaporation. If that is for capacitive droplet accelerometer, a thin insulating layer needs to be doped on. Final step would be encapsulation as forming a square channel. The whole processes are illustrated in Fig 6.4 - 6.6.

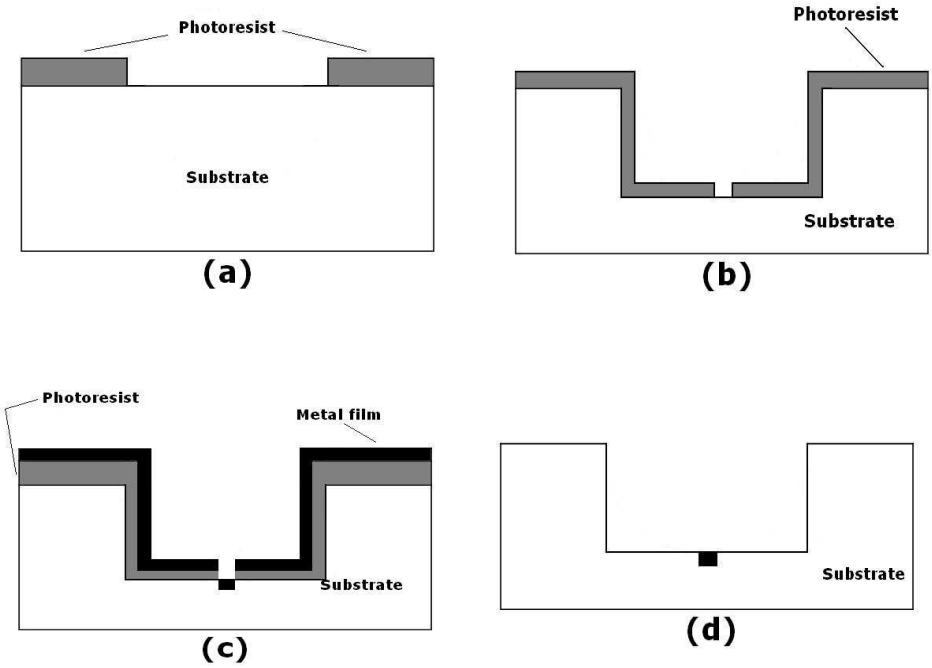

Figure 6.4: Fabrication Process of Square Duct

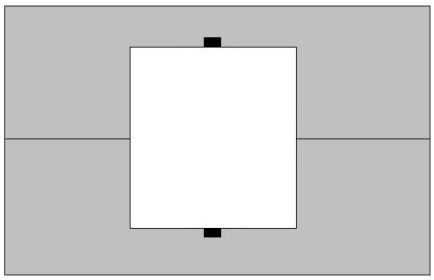

Figure 6.5: Cross Section of Accelerometer

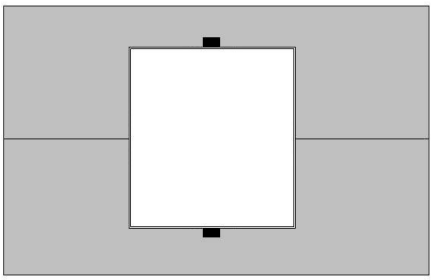

Figure 6.6: With An Insulating Layer

Chapter 7

Conclusions and Future Work

Our motivation in this thesis is to build a basis for the design of liquid-droplet accelerometers. More specifically, we want to design a capacitive or resistive liquid-droplet accelerometer with selected liquids and materials. This has been studied by research, CFX modeling and experiment. Here is a summary of the thesis.

First of all, a group of micro-accelerometers were studied, including conventional and non-conventional ones.

Next, a proposed structure was presented followed by a series of possible measurements. We considered one idealization of the structure: a sealed duct where fluid is placed in the middle supported by an air cushion on each side. Air cushions function as springs by hydraulic pressure in this airtight duct. Two ways to detect fluid displacement are resistance and capacitance.

On the basis of these assumptions, the governing equations were derived, to pursue possibility of our designs. As well, response time and sensitivity equations were explored. Surface tension and contact angle , two important aspects, were addressed here for a better understanding of our design.

Transient performance of the accelerometer was predicted in ANSYS CFX by simulating a 30mm long and 3mm diameter circular tube with mercury as the working fluid. The result was in good agreement with our prediction. Then a set of steady-state simulations for different tube sizes and shapes were investigated to confirm published correlations for fluid flow and give a basis for predicting response time.

A series of experimental studies were executed in order to verify numerical results, including transient and steady flow experiments. A few comparisons were drawn by figures.

At the end, the choice of materials and fabrication process were discussed for resistive and capacitive design. Although liquid/duct surface combinations were found for both designs, we did not find a combination with the right properties to give high sensitivity in a capacitive design. For a resistive design, galinstan on a gallium-oxide-coated surface is predicted to give high sensitivity, low response time, and low toxicity.

Based on these results, we have established a design for a liquid-drop accelerometer. In future, we will try to build a prototype using galinstan with gallium oxidation to test them.

Appendix A

Complete Simulation Procedures in ANSYS CFX

Fluid-droplet accelerometer simulations in ANSYS CFX are the most important numerical basis for us to develop this design. ANSYS CFX is a complex, powerful package, and considerable case is needed to obtain reliable results. This appendix should be regarded as a user's guide.

A.1 ANSYS CFX Model

The CFX model of the liquid-droplet accelerometer is shown in Figure A.1. It is a 3-D cylinder, modeled as a duct. In this figure, the liquid and gaseous working fluids are not defined yet - they are not defined at the meshing stage but later on.

A.1.1 Meshing

The CFX model can be meshed automatically in ANSYS based on requirements. The meshing method in ANSYS is a key factor to pursue a more accurate and realistic result. Manually defining the sizes of elements in the radial and circumferential directions creates a mesh with more uniform elements and therefore improved accuracy.

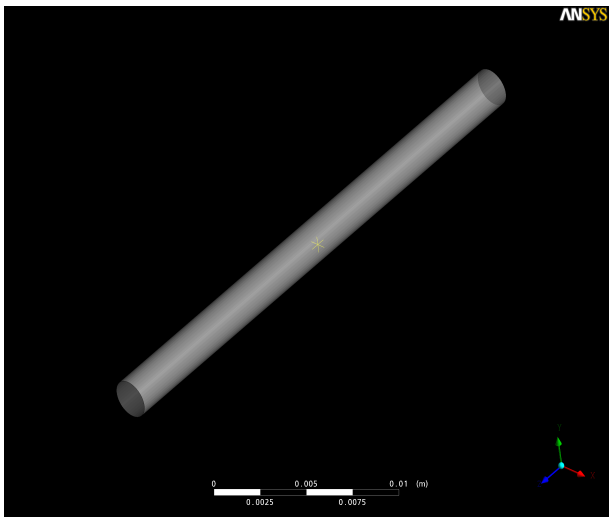

Figure A.1: The Model in CFX

In this case, one half of the cross-section of the cylinder is built and meshed, then the other half area is formed by reflecting the meshed half. After constructing the whole cross-section area, the Extrude function is used to turn the 2-D planar circle into a 3-D well-meshed cylinder. This 3-D cylinder is guaranteed to be meshed evenly, equally and uniformly everywhere. According to the theory of finite element analysis, the more finite elements defined in the model, the more accurate result can be produced, however the more capacity and time it takes in the simulation by computers. Once the mesh has been produced in ANSYS, it is written to disk as a '.cdb' file. This file is read by ANSYS-CFX, a separate program.

A.2 CFX-Pre

After the mesh has been created in ANSYS and read into ANSYS CFX, the fluids used in the simulation must be defined, This is done in the CFX-Pre.

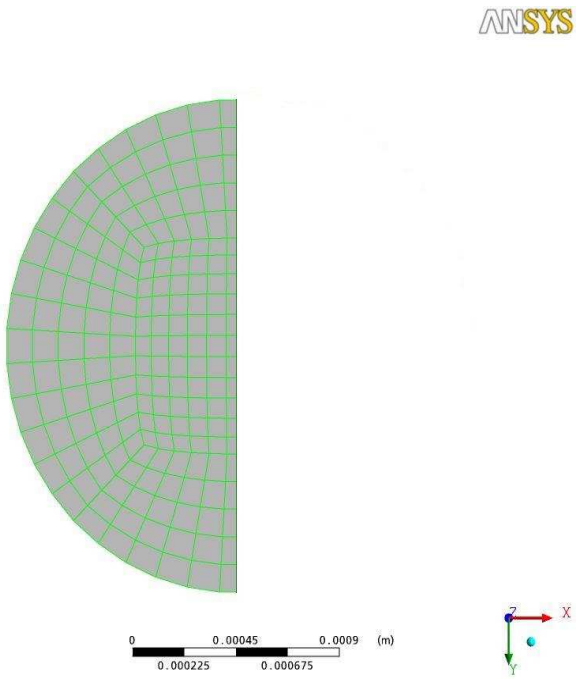

Figure A.2: Half Mesh

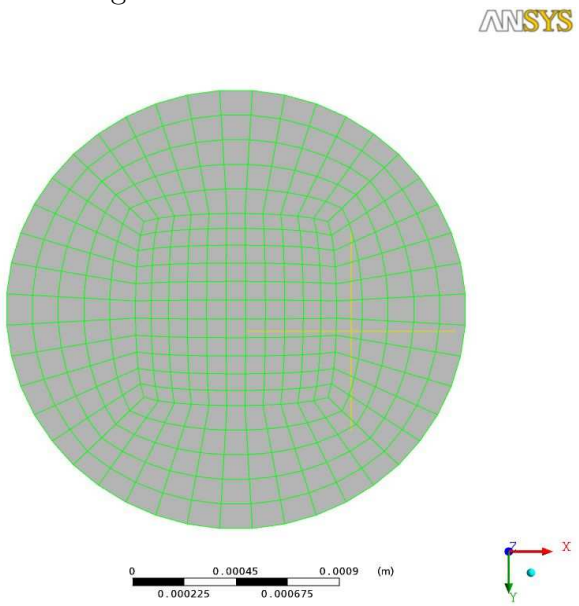

Figure A.3: Full Mesh

A.2.1 Materials

In the outline menu, we can see that 'Materials' item is included. Right click on it, and choose 'Import Library Data'. A window named 'Select Library Data to Import' prompts the user to select appropriate materials, we choose 'Air Ideal gas' in Air Data column and 'Mercury' in Constant Property Liquids column. The reason why 'Air Ideal Gas' is selected, rather than 'Air at 25C', is that 'Air Ideal Gas' enforces the ideal gas equation, $PV = nRT$. This ensures that gas pressure increases when the gas is compressed or heated. After choosing them, click 'Ok' to return to the outline menu, so the materials are ready to be used.

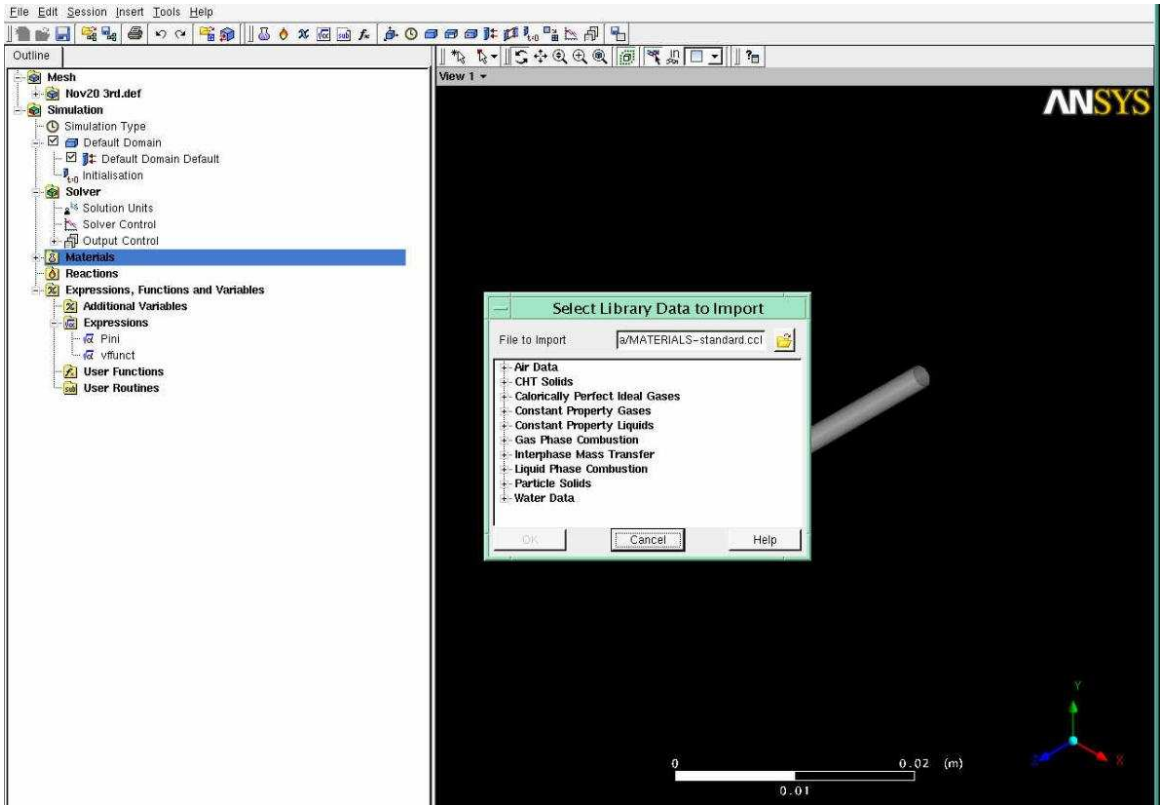

Figure A.4: Materials

A.2.2 Simulation Type

Our simulation type is 'Transient'. The choice of transient simulation or static depends on the situation to be analyzed. For example, an analysis using a steady-state simulation is often satisfactory for monitoring global quantities. A transient simulation can be used to observe transient effects, such as recirculation zones. In our case, a static simulation would tell us the distance the fluid is displaced, but a transient simulation is needed to tell us the response time.

In transient mode, both physical timesteps and the maximum number of coefficient iterations per timestep are needed. The selected timesteps need to be based on the timescale of the transient behavior that we want to resolve in the flow simulation. However, large numbers of coefficient iterations may not increase the accuracy of the results at each timestep and demand large amount of CPU time. Therefore it is necessary to make a compromise between timestep size, number of coefficient iterations and residual tolerance to get the most cost-effective solution.

In this simulation, the initial time started from 0 second, and the time duration is 1 second. Time duration being 1 second is an estimate based on the transient features, which means the whole performance would possibly end within 1 second. Besides the initial time and time duration, the timestep is set up as 0.0001 second. This is a very short timestep, and as a result, the simulation takes a long time to complete. But it becomes unstable if a longer step is used.

A.2.3 Default Domain

Under the menu item 'Default Domain', there are several menus representing different aspects of domain.

1. General Options
The first simulation, only has one direction of acceleration (Buoyant Force), along Z, the same direction as the axis of cylinder. Besides Buoyant Force settings, 'buoyant

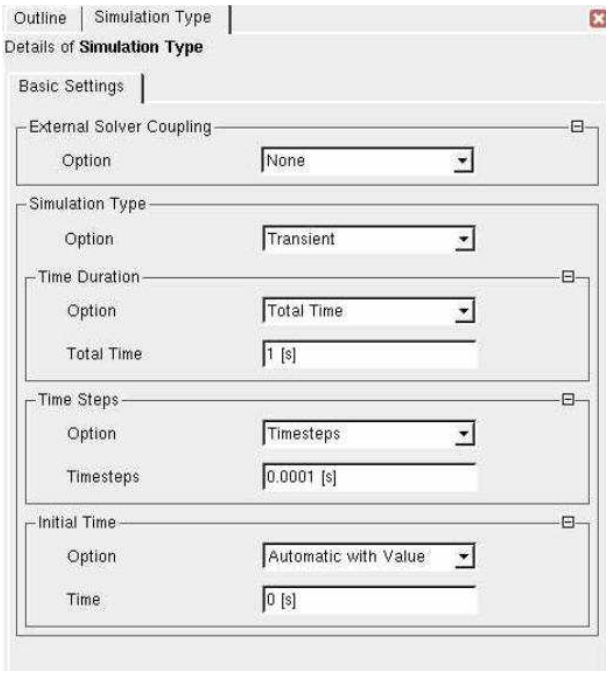

Figure A.5: Simulation Type

reference density', another crucial element, defines the difference in density between phases that produces a buoyant force. For free surface cases, such as this one, the density of the lighter fluid should be chosen since this gives an intuitive interpretation of pressure, constant in the light fluid and hydrostatic in the heavier fluid. It benefits the post processing by simplifying pressure initial conditions, pressure boundary conditions and force calculations. In our simulation, the density of Air Ideal Gas, which is 1.185 kg/m^3 at atmospheric pressure, is much smaller than the density of mercury. The extreme difference - over a factor of 10,000 - between the densities of the two fluids is one of the reasons this simulation converges so slowly.

As shown in Figure A.6, the domain type is fluid domain. The reference pressure is applied to Air cushion on both ends of tube, and here is entered as 2000 Pa.

2. Fluid Models

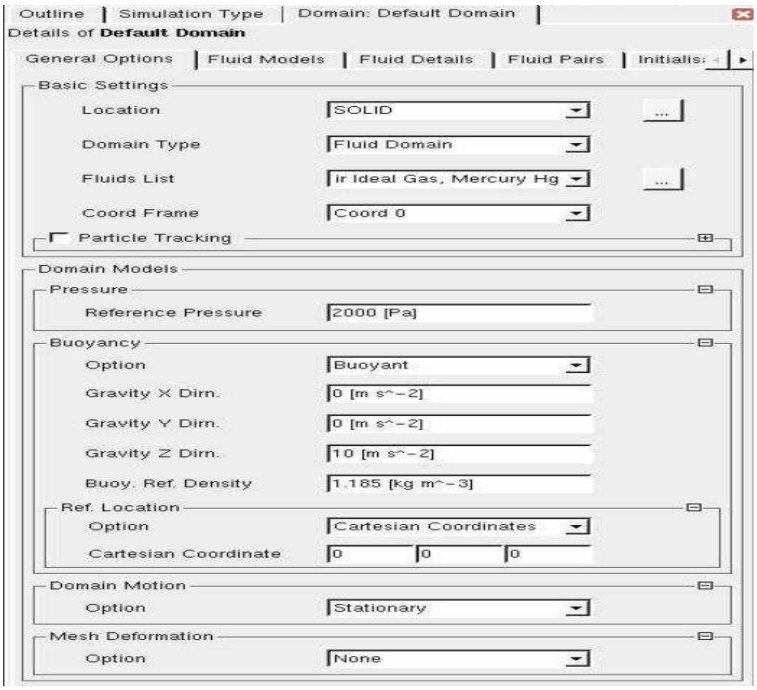

Figure A.6: General Options

In Fluid Models section, the simulation is defined as Homogeneous model, Free Surface and Laminar Flow.

The homogeneous model can be used when the interface between the two phases remains well defined and none of the dispersed phase becomes entrained in the continuous phase. For this simulation, the interface between air and mercury is maintained- we do not expect an air/mercury froth or foam- so it belongs to homogeneous model.

'Free Surface flow model' refers to a multiphase flow situation where the phases are separated by a distinct interface, which accurately describes the state between air and mercury in our simulation.

Laminar flow is governed by the unsteady Navier-Stokes equations. It typically applies at low Reynold's number flows. Energy transfer in the fluid is accomplished by molecular interaction (diffusion). In the design of droplet accelerometer, mercury

will smoothly move along duct forced by acceleration. The duct dimensions are small enough that the flow will always be laminar.

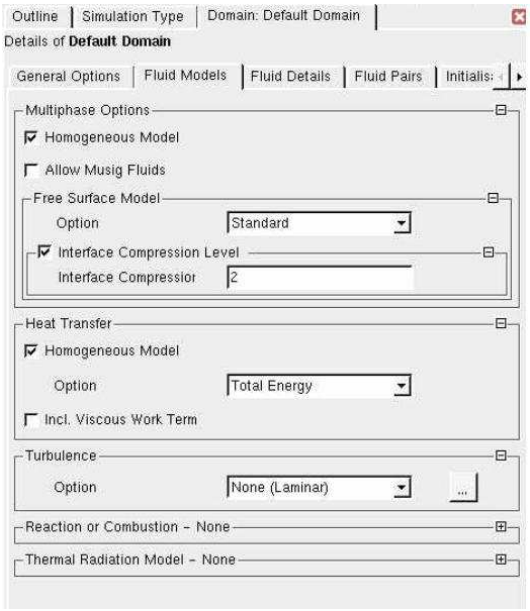

Figure A.7: Fluid Models

3. Fluid Details

In the Fluid Details settings, both Air Ideal Gas and Mercury are defined as continuous fluids where a continuous fluid is one which forms a continuous connected region as opposed to a spray or a foam. Density Difference is the default option for all multiphase flows, and means that the buoyancy force is modeled by considering the difference in density between phases. The reason why it is selected is that when mercury moves towards to one side, the air cushion is compressed on that side. Hence its density must be treated as variable.

4. Fluid Pairs

The first menu item in Fluid Pairs defines the surface tension coefficient. Surface tension is the force that holds the interface together. If an interface is cut, the magnitude of the surface tension force per unit length is called the surface tension coefficient.

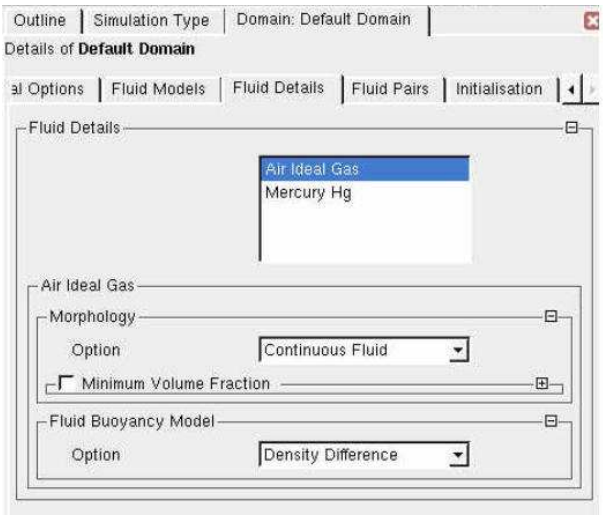

Figure A.8: Fluid Details

The surface tension model used in ANSYS CFX is based on the Continuum Surface Force model, which models the surface tension force as a volume force concentrated at the interface, rather than a surface force. Consider the free surface interface shown in the Figure A.9 below:

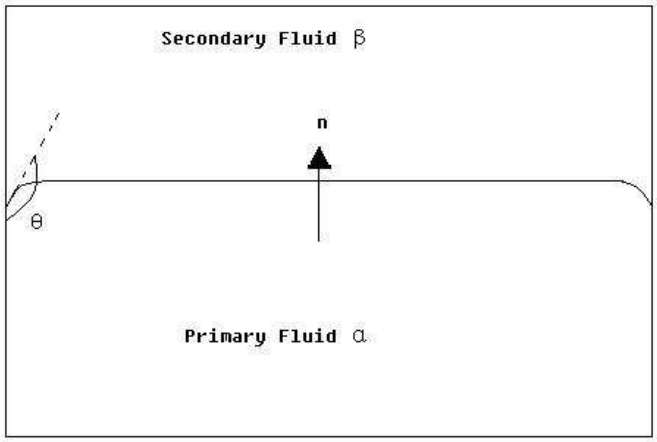

Figure A.9: Free Surface Interface

Define a Primary Fluid α (the liquid phase) and a Secondary Fluid β (usually a gas phase). The surface tension force given by the Continuum Surface Force model is:

$$F_{\alpha\beta} = f_{\alpha\beta}\delta_{\alpha\beta} \tag{A.1}$$

Where:

$$f_{\alpha\beta} = -\sigma_{\alpha\beta}k_{\alpha\beta}n_{\alpha\beta} + \nabla_s\sigma \tag{A.2}$$

$$\delta_{\alpha\beta} = |\nabla r_{\alpha\beta}| \tag{A.3}$$

Where δ is the surface tension coefficient, $n_{\alpha\beta}$ is the surface normal vector pointing from the primary fluid to the secondary fluid, ∇_s is the gradient operator on the interface and k is the surface curvature defined by:

$$k_{\alpha\beta} = \nabla n_{\alpha\beta} \tag{A.4}$$

The two terms summed on the right hand side of Equation A.2 reflect the normal and tangential component of the surface tension force respectively. The normal component arises from the interface curvature and the tangential component from variations in the surface tension coefficient.

The $\delta_{\alpha\beta}$ term is often called the interface delta function, being zero when away from the interface. Thereby, ensuring that the surface tension force is active only near to the interface.

Surface tension has a number of important physical effects, including:

• If the interface is curved, it induces a force normal to the interface. For a droplet at rest, this induces a pressure rise within the droplet of $\triangle_p = \sigma k$, where k is the droplet curvature. The effect of this normal force is to smooth regions of high curvature; it tends to reduce the surface area of droplet.

• When the free surface interface touches a wall, the wall may attract the liquid (wetting wall) or repel the liquid (non-wetting wall). In a static situation, the wall contact angle may be measured. This phenomenon, known as wall adhesion, gives rise to effects such as the meniscus and capillary rise in tube.

When surface tension is enabled, a surface tension coefficient must be specified. In this simulation, we used a value of $0.48N/m$. If the surface model is activated, double precision is often required to avoid round-off errors in the curvature calculation. This procedure comes at the end of CFX-pre.

When evaluating the interface normal vector for the curvature and surface tension force, it is usually to take the gradient of a smoothed volume fraction field. The volume fraction smoothing method could be optionally set in our simulation, including None, Laplacian and Volume-Weighted. Laplacian, the one we chose, is slightly more accurate, although it takes longer time to simulate than Volume-Weighted. Curvature Under Relaxation Factor is used for under-relaxing the curvature. The default value is 1, but for flows strongly driven by surface tension, it may be useful to use a smaller value. Considering our case, mercury and air as multiphase, 0.8 was input as try-out, could be modified for comparison.

5. Intialisation
In this section, the Static Pressure is set as 0 Pa. ANSYS CFX solves for the relative Static Pressure in the flow field , that is related to Absolute Pressure by:

$$P_{abs} = P_{stat} + P_{ref} \tag{A.5}$$

In some situations, the true pressure is required to calculate fluid properties. For example, if the fluid is compressible, the density depends on the true pressure rather than the motion pressure. In addition, it is often useful to visualize the true pressure. According to our current simulation, it does not have hydrostatic contribution when mercury is at rest. So Static Pressure is 0 Pa and Absolute Pressure equals Reference

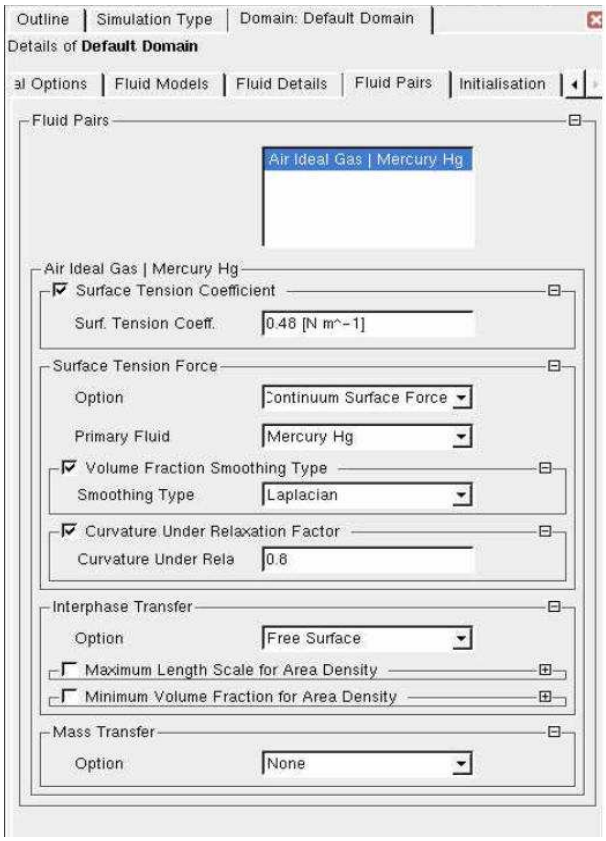

Figure A.10: Fluid Pairs

Pressure.

As noted, the initial mesh does not specify which regions of the duct are occupied by air and which by mercury. We specify this by setting the volume fraction. In the duct, mercury is filled and placed in the center and the rest of space is filled with air. Therefore, either mercury or air volume fraction needs to be input, the other would be automatically recognized. In this case, the volume fraction of air ideal gas is set as Automatic and mercury as:

$$step(0.02 - z/1[m]) * step(z/1[m] - 0.01) \tag{A.6}$$

This function is plotted in Fig A.11

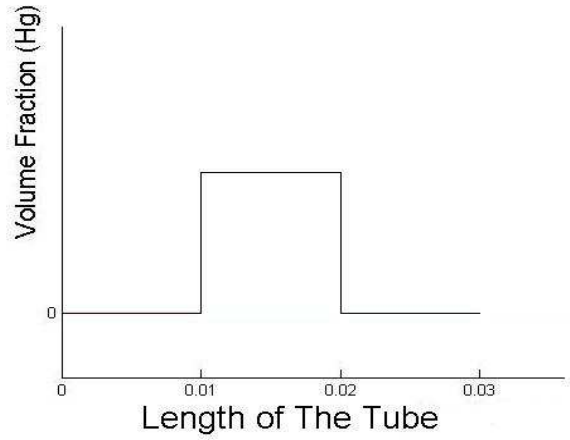

Figure A.11: Hg Volume Fraction Function

A.2.4 Default Domain Default

This section is for definitions of Boundary Details. First of all, our simulation's boundary type is "Wall". In ANSYS CFX, a fluid boundary is an external surface of a fluid domain and can be of the following types:

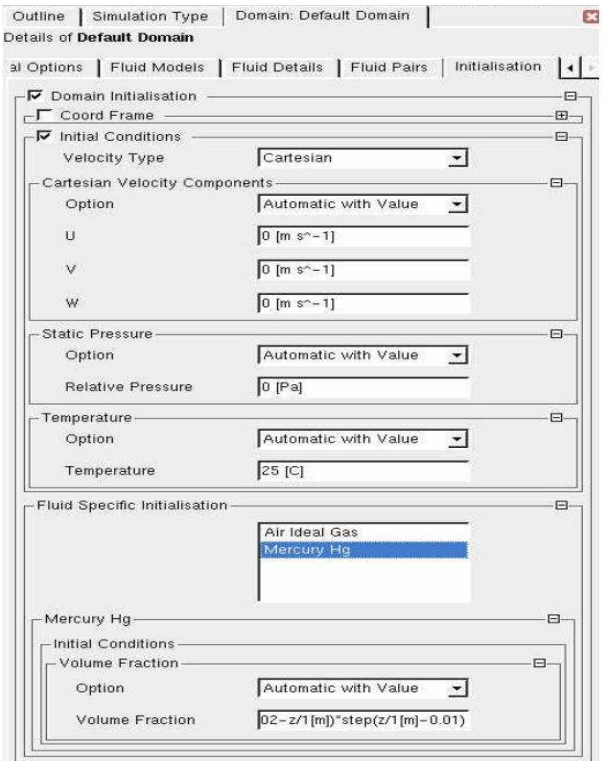

Figure A.12: Initialisation

• Inlet: Fluid predominantly flows into the domain

• Outlet: Fluid predominantly flows out of the domain

• Wall: Impenetrable boundary to fluid flow

• Symmetry Plane: A plane of both geometric and flow symmetry

We have a sealed duct, so all the boundaries are of type "Wall". The boundary condition of Wall specifically includes No Slip and Free Slip Wall options. Free Slip Wall conditions mean:

• On free slip wall the shear stress is set to zero, so that the fluid is not retarded

• The velocity normal to the wall is also set to zero

• The velocity parallel to the wall is calculated during the solution

In the simulation that we design, the shear stress can not be ignored, on the contrary it is the most important factor that decides whether the design can be successful or not. Therefore, No Slip is chosen for "Wall Influence On Flow". Since the wall is no slip for the mercury, the contact angle between mercury and wall must be specified. For non-wetting wall, this angle is greater than 90 degrees. After checking mercury database, the wall contact angle is 140 [degree].

A.2.5 Solver Control and Output Control

We have now finished defining simulation conditions. Some additional parameters must be set for better results during CFX processing. In Solver Control - Advanced Options, check Multiphase Control and select "Coupled" for "Volume Fraction Coupling". While in Output Control - Monitor, we need to set up Monitor Point 1 in

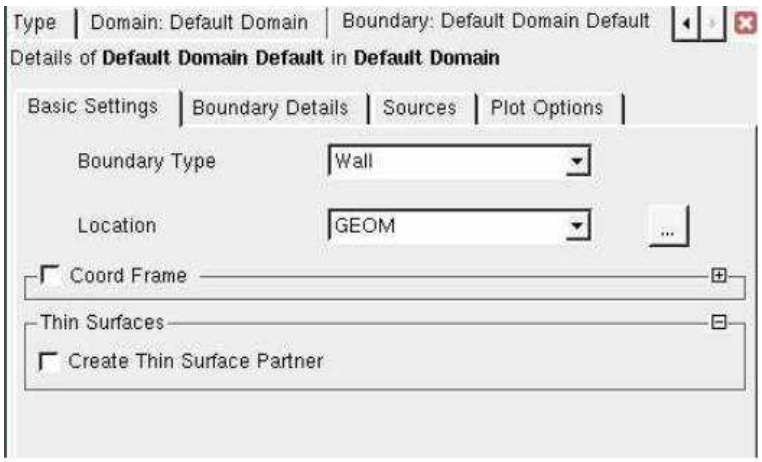

Figure A.13: Basic Settings

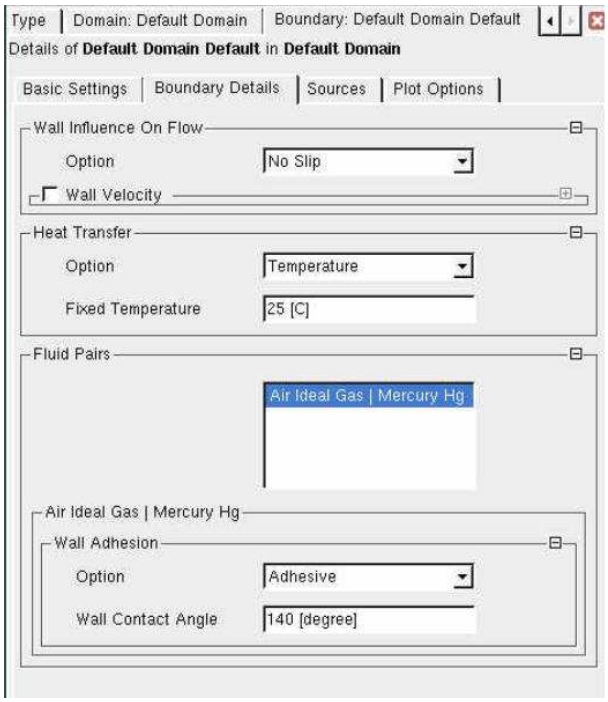

Figure A.14: Boundary Details

order to observe the value and plot during CFX solving. Any values shown in the Output Variables List from this point could be selected. Here we choose Mercury Hg. Velocity as observation.

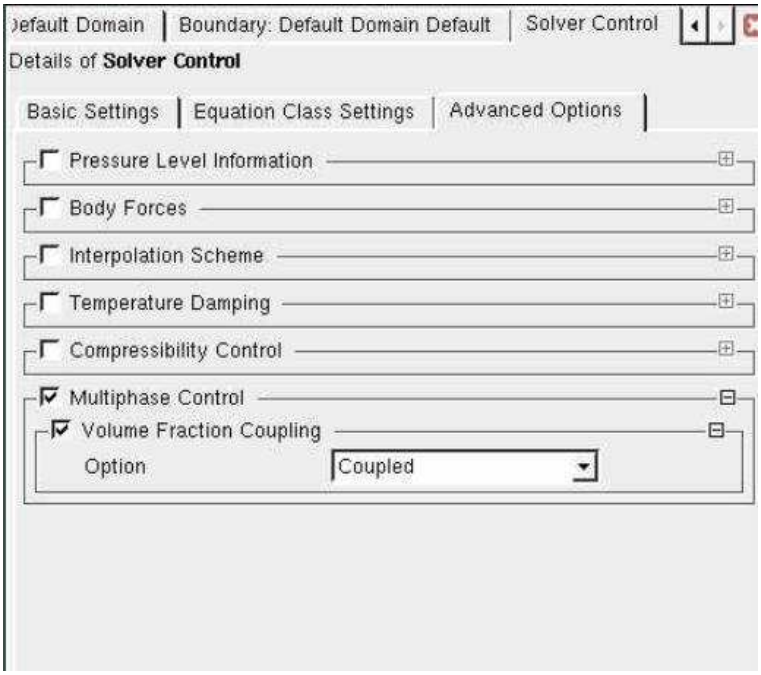

Figure A.15: Advanced Options

A.3 CFX-Solver

After setting all parameters in CFX Pre to define a circumstance as real as possible, the next step is to let ANSYS CFX to calculate and simulate in the solver. The last parameter is to give the order "Run", where "Double Precision" has to be activated. Double Precision is a recommended practice for free surface flow, because it sometimes helps reduce spurious oscillations at the free surface to avoid round-off errors.

The duration of the simulation relies on the mesh of the entire structure, the complication of the simulation itself and the time duration of the process. In our first try,

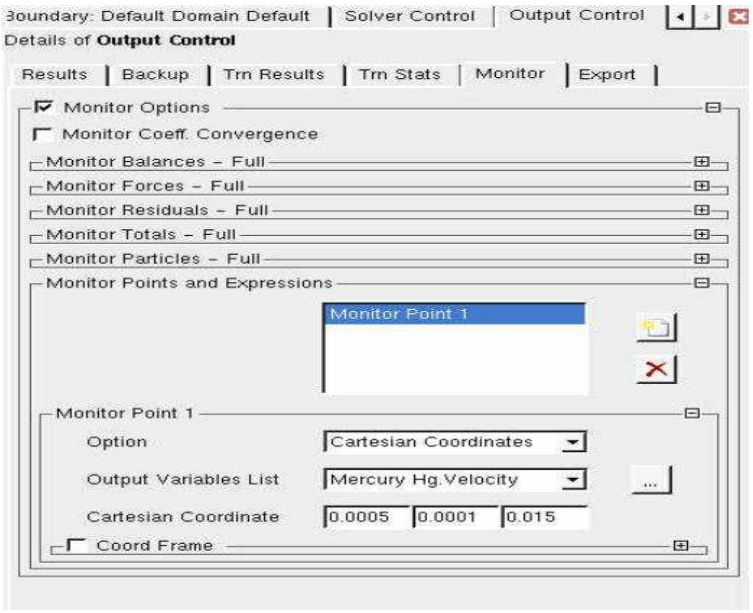

Figure A.16: Monitor

a moderate mesh was adopted, which is enough to illustrate the general motion of mercury, although the results have blurred edges. It also is a transient effect. Therefore the whole time duration is within 1 second. After successfully completing the simulation, it spent over a total of 240 hours and occupied 80 GB space for data storage.

A.4 CFX-Post

Once simulation is finished, CFX-Post will automatically open for post-processing of results. Click 'Location' at the top of menus and choose 'Plane' to prompt a window. The Details of Plane will display. Click 'colour' and change 'Mode' to 'Variable', then in the 'Variable' box, select any parameters you want to see in the plane. Click 'Apply' to let CFX show the pictures.

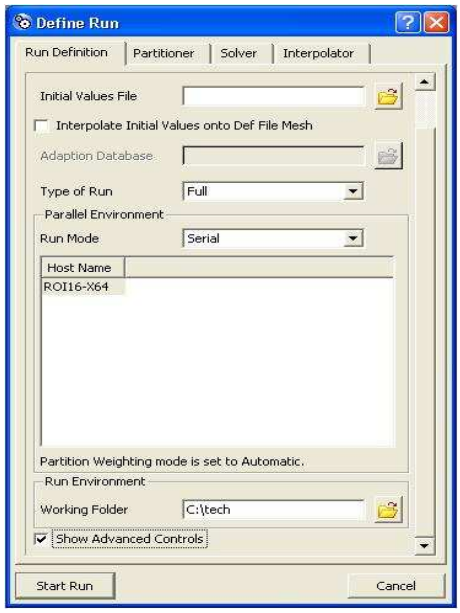

Figure A.17: CFX Solver Control Panel

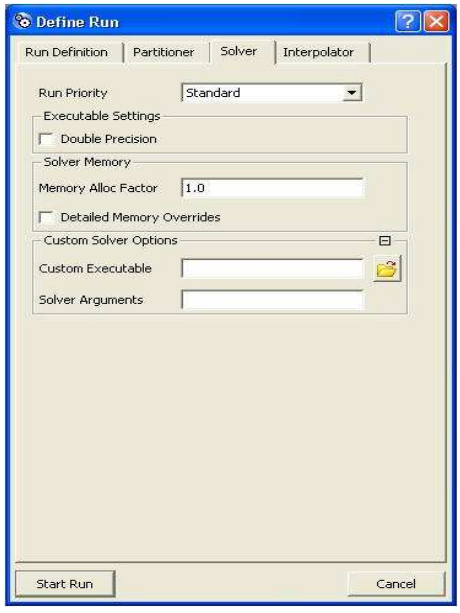

Figure A.18: Double Precision

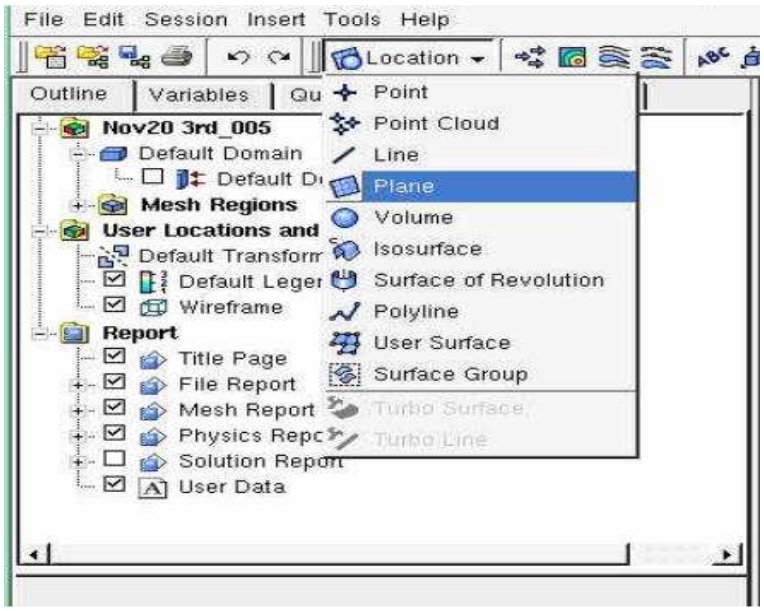

Figure A.19: CFX Post Control Panel

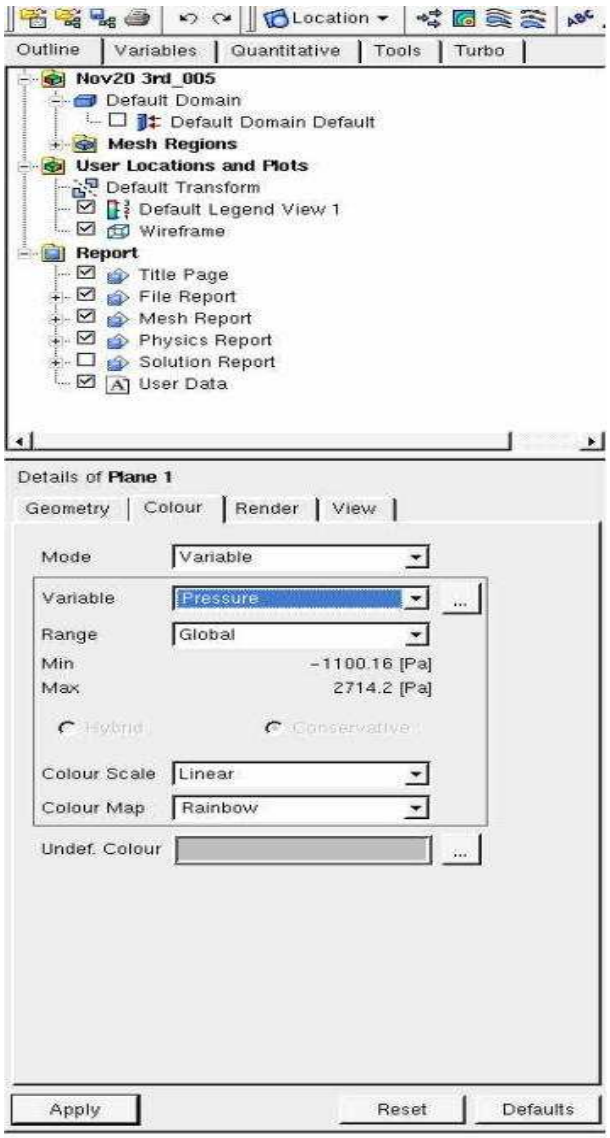

Figure A.20: Post Details

Bibliography

[1] A. B. Wu, J. Jones, *Analysis of Liquid-filled Convective Micromachined Accelrometer*, International Conference for Upcoming Engineers, Waterloo, Ontario, May, 2006.

[2] A. B. Wu, *Thermal Drift in Convective Micromachined Accelerometer*, MASc Thesis, Simon Fraser University, August 2007.

[3] A. B. Wu, J. Jones, *Thermal Drift of Convection-Based Microthermal Accelerometer*, ASME International Mechanical Engineering Congress and Exposition, Seattle, Washington, November 2007.

[4] A. Beliveau, G. Spencer, *Evaluation of MEMS Capacitive Accelerometers*, Design and Test of Computers, IEEE 1999.

[5] A. Leung, J. Jones, E. Czyzewska, J. Chen, and M. Pascal, *Micromachined Accelerometer with No Proof Mass*, in Technical Digest of Int. Electron Device Meeting (IEDM97), Washington, D.C., Dec. 1997, pp899-902.

[6] ANALOG DEVICES, *Low Cost Low Power Instrumentation Amplifier AD620*, http://www.analog.com, consulted August 2008.

[7] A. Iula, N. Lamberti, *Analysis and Experimental Evaluation of a New Planar Piezoelectric Accelerometer*, Transaction on Mechatronics, Vol. 4, No. 2, June 1999.

[8] A. Salian, H. Kulah, *A Hybrid Silicon Microaccelerometer System with CMOS Interface Circuit*, 43rd IEEE Midwest Symp. On Circuits and Systems, MI, Aug 8-11. 2000.

[9] B. E. Boser, R. T. Howe, *Surface Micromachined Accelerometer*, IEEE Journal of Solid-State Circuits, Vol. 31, No. 3, March 1996.

[10] G. Q. Hu, W.H. Liao, *A Feasibility Study of A Microaccelerometer with Magnetorheological Fluids*, International Conference on Robotics, Intelligent Systems and Signal Processing, Changsha, China, October 2003.

[11] H. Yang, H. Guo, *Design of A Bulk-Micromachined Piezoelectric Accelerometer*, Ultrasonic Symposium, IEEE 2007.

[12] J. Chae, H. Kulah, K. Najafi, *A Hybrid Silicon-On-Glass Lateral Micro-Accelerometer with CMOS Readout Circuitry*, 7803-7185-2/02 2002 IEEE.

[13] J. Chae, H. Kulah, K. Najafi, *An In-Plane High-Sensitivity, Low-Noise Micro-G Silicon Accelerometer*, Journal of Microelectromechanical Systems, Vol. 14, No. 2, April 2005.

[14] J. Chae, H. Kulah, K. Najafi, *A Monolithic Three-Axis Micro-g Micromachined Silicon Capacitive Accelerometer*, Micro Electro Mechanical Systems, 2003. MEMS-03 Kyoto.

[15] J. Lynch, A. Partridge, K. H. Law, *Design of Piezoresistive MEMS-Based Accelerometer for Integration with Wireless Sensing Unit for Structure Monitoring*, Journal of Aerospace Engineering, ASCE, July 2003.

[16] K. Y. Fu, Y. F. Mei, G. J. Wan, *Surface Composition and Surface Energy of Teflon Treated by Metal Plasma Immersion Ion Implantation*, Surface Tension 573 (2004) 426-432.

[17] K. Najafi, J. Chae, H. Kulah, *Micromachined Silicon Accelerometer and Gyroscopes*, Intelligent Robots and Systems, 2003.

[18] K. Szaniawski, A. Napieralski, P. Sekalski, *Design of A Prototype of A 3-Axis Capacitive Acceleration Sensor*, International Conference On Microelectronics, May, 2004.

[19] K. Y. Fu, Y. F. Mei, G. J. Wan, *Surface Composition and Surface Energy of Teflon Treated by Metal Plasma Immersion Ion Implantation*, Surface Science 573 (2004) 426-432.

[20] L. Lin, J. Jones, *A Liquid-Filled Buoyancy-Driven Convective Micromachined Accelerometer*, Journal of Microelectromechanical Systems, Vol. 14, No. 5, October 2005.

[21] L. Lin, *Design and Analysis of Microthermal Accelerometer*, Ph.D Thesis, Simon Fraser University, March 2004.

[22] M. Bahrami, M. M. Yovanovich, J. R. Culham, *Pressure Drop of Fully-Developed, Laminar Flow in Microchannels of Arbitrary Cross-Section*, 3rd International Conference on Microchannels and Minichannels, June 13-15, 2005, Toronto.

[23] R. Amarasinghe, D. V. Dao, T. Toriyama, *Simulation, Fabrication and Characterization of A Three-Axis Piezoresistive Accelerometer*, Smart Mater. Struct. 15(2006) 1691-1699.

[24] Richard C. Jaeger, *Introduction to Microelectronic Fabrication*, Prentice Hall, 2002.

[25] S. J. Lee, D. W. Cho, *Development of A Micro-Opto-Mechanical Accelerometer Based On Intensity Modulation*, Microsystem Technologies 10 (2004) 147-154.

[26] Y. Yee, J. Bu, K. Chun, *An Integrated Digital Silicon Micro-Accelerometer with MOSFET-Type Sensing Elements*, J. Micromech. Microeng. 10 (2000) 350-358.

[27] *Dielectric Constants Chart*, www. asiinstr.com/technical/Dielectric20Constants.htm.

[28] *Geratherm Medical AG*, www.geratherm.com/en/unternehmen/.